Journal of Sound and Vibration 329 (2010) 1717–1742

Contents lists available at ScienceDirect

Journal of Sound and Vibration

journal homepage: www.elsevier.com/locate/jsvi

# A shell model for tyre belt vibrations

C. Lecomte [a], W.R. Graham [a,*], M. Dale [b]

[a] University of Cambridge, Department of Engineering, Trumpington Street, Cambridge CB2 1PZ, UK
[b] Jaguar LandRover Ltd, Gaydon Technology Centre, Gaydon, Warwickshire CV35 0RR, UK

ARTICLE INFO

*Article history:*
Received 12 February 2009
Received in revised form
17 August 2009
Accepted 17 November 2009
Handling Editor: A.V. Metrikine
Available online 6 January 2010

ABSTRACT

We present a new formulation for the prediction of tyre belt vibrations in the frequency range 0–500 Hz. Our representation includes the effects of belt width, curvature and anisotropy, and also explicitly models the tyre sidewalls. Many of the associated numerical parameters are fixed by physical considerations; the remainder require empirical input. A systematic and general approach to this problem is developed, and illustrated for the specific example of a Goodyear Wrangler tyre. The resulting predictions for the radial response to radial forcing show good correspondence with experiment up to 300 Hz, and satisfactory agreement up to 1 kHz.



## 1. Introduction

Vehicle road noise is generated by the high-frequency tyre vibrations that arise due to the unsteady contact of the tread pattern with the textured road surface. It is transmitted to the cabin via two routes: structure-borne and air-borne. These components are thought to be important in the frequency ranges up to 500 Hz, and from 500–2000 Hz, respectively [1]. The work presented here is part of a project to improve prediction of the structure-borne component at the vehicle design stage. More specifically, it aims to provide a set of tyre impulse responses to point forcing, to be used subsequently in a time-domain, convolution-based simulation of the rolling tyre.

Finite-element calculations at these frequencies are still extremely expensive, if not prohibitive. This problem can be ameliorated by employing the 'waveguide FEA' approach (e.g. [2]), in which case successful tyre vibration modelling is possible [3]. Nonetheless, the computational requirements remain relatively high and the model is complex, both undesirable features for a design tool. We therefore seek a simpler representation of the tyre structure.

Pioneering work in this area has been carried out by Kropp and his co-workers, who have modelled the tyre as a flat plate on a spring bedding. Their most recent formulation [4] allows the plate to support in-plane, flexural and shear waves. Although initially reported agreement with experiment was only fair, the subsequent development by Andersson and Larsson [5] shows excellent fidelity above 100 Hz. Below this frequency, the absence of curvature from the representation renders the model invalid.

Real tyres are strongly anisotropic, and this feature was included in a plate model by Graf [6]. She found it impossible to specify a set of elastic parameters that would match both high- and low-frequency behaviour, but nonetheless achieved accurate radiated noise predictions for 500–1000 Hz.

A satisfactory representation of curvature effects is clearly a pre-requisite at the lower frequencies. Campanac et al. [7] have presented a one-dimensional, 'ring', model meeting this requirement, while Kim and Bolton [8] have applied Soedel's

* Corresponding author.
*E-mail address:* wrg@eng.cam.ac.uk (W.R. Graham).

0022-460X/$ - see front matter © 2009 Elsevier Ltd. All rights reserved.
doi:10.1016/j.jsv.2009.11.022

equations for a cylindrical shell [9] to the same effect. However, neither of these approaches has been experimentally validated.

In contrast, Pinnington has developed [10], and tested [11], a curved-plate tyre model. The plate admits flexural, in-plane longitudinal and in-plane shear waves, and is coupled to an explicit sidewall representation. For a suitably chosen set of material properties, good agreement with measured point and transfer mobility amplitudes was achieved, especially for line excitation in the 100–400 Hz frequency range.

For our work, we require both low- and high-frequency fidelity (the former to ensure accurate simulation of the mean tyre deflection in rolling), and an explicit sidewall representation (to extract the unsteady force on the wheel hub). Among the models discussed here, the flat-plate idealisations are invalid at lower frequencies, while Kim and Bolton's formulation assumes isotropy and considers only simply-supported belt edges. The closest to fulfilling our requirements is Pinnington's, but we regard this as unsuited to our purposes, for two reasons. The first, and most important, is that Pinnington does not properly represent the influence of the sidewalls on the belt vibration. Instead, he assumes a restrictive form for the cross-belt displacement, in terms of a non-general Fourier series, and then assigns an additional impedance, due to the sidewalls, to each Fourier mode. Even if one were to accept the arbitrarily imposed form for the belt shape, we believe that the Fourier modes should be coupled by the sidewall impedance (we have been unable to reproduce Pinnington's uncoupled form, Eq. (21) of [10]). The second reason for not using the model is its inclusion of a shear wave mode, which is not relevant until frequencies in excess of 2 kHz [4]. Our ultimate aim is to produce a tool that can be used in preliminary design, and we therefore seek to minimise the number of parameters requiring experimental determination, of which (in [10]) the shear stiffness is one.

The Pinnington model could, of course, be modified to eliminate the shear wave. Rectification of the sidewall coupling formulation would be awkward though, requiring explicit expressions for the belt-edge stress resultants. These quantities are notoriously difficult to obtain correctly from equilibrium considerations; they can, however, be found reliably via energy-based methods. For this reason, we have chosen to develop our model—an orthotropic cylindrical shell representation of the tyre belt, coupled to a membrane representation of the sidewalls—*ab initio*.

The paper is structured as follows. In Section 2 we derive the governing equations using a variational analysis and set out the numerical approach used to solve them. Experiments carried out for validation and parameter identification purposes are described in Section 3. Finally, in Section 4, we present a systematic parameter identification procedure, and compare the resulting predictions with the measurements.

## 2. Theoretical analysis

Here we set out the theoretical basis of the paper. We start with the analysis leading to the equations governing belt motions, and then proceed to the simpler case of the sidewall. Finally, we formulate the impulse response of the coupled belt/sidewalls system.

### 2.1. The belt model

As the eventual aim of the calculation is to resolve forces at the tread-block level, the natural frame of reference is one rotating with the tyre. This, then, precludes straightforward consideration of the belt vibrations as perturbations to the loaded shape. Instead, they can be viewed as displacements from the original, cylindrical geometry, with these displacements consisting of a repeatable, periodic component (associated with the loaded shape) and a stochastic element (due to varying contact with the rough road surface). Once accepted, this approach has two advantages: the loaded tyre shape need not be pre-calculated, as it is found implicitly in the rolling simulation (see, for example, [12]), and the undeformed geometry takes a simpler form.

Nonetheless, the equations of motion and the boundary stress resultants for vibrations of an orthotropic cylindrical shell subject to internal pressure and axial pre-stress do not appear to have been set out explicitly in the published literature. Here, we shall derive them on the basis of a variational formulation. The main advantage of this method is that it ensures consistency between the equations of motion and the boundary stress resultants, a feature that is not easily achievable with a direct approach.

The starting point of the analysis is the definition of suitable coordinates, and of the deformed belt shape (Section 2.1.1). The belt velocity and kinetic energy then follow straightforwardly (Section 2.1.2). The potential energy calculation is more involved, involving not only extensional and bending stiffness terms, but also contributions from the pre-tensions and internal pressure (Section 2.1.3). Finally, the kinetic and potential energy expressions are combined in the variational analysis to yield the desired governing equations (Section 2.1.4). These are compared with previous authors' formulations in Section 2.1.5, and solved formally in Section 2.1.6.

#### 2.1.1. Geometrical considerations

Fig. 1 shows the undeformed, cylindrical belt geometry and associated coordinate axis vectors. The Cartesian set $(\mathbf{e}_x, \mathbf{e}_y, \mathbf{e}_z)$ is fixed in the inertial reference frame moving with the axle, pointing, respectively, in the axial, downwards and complementary directions. The rectangular polar set $(\mathbf{e}_r, \mathbf{e}_\theta, \mathbf{e}_x)$ rotates with the belt. For a given material point on the tyre,

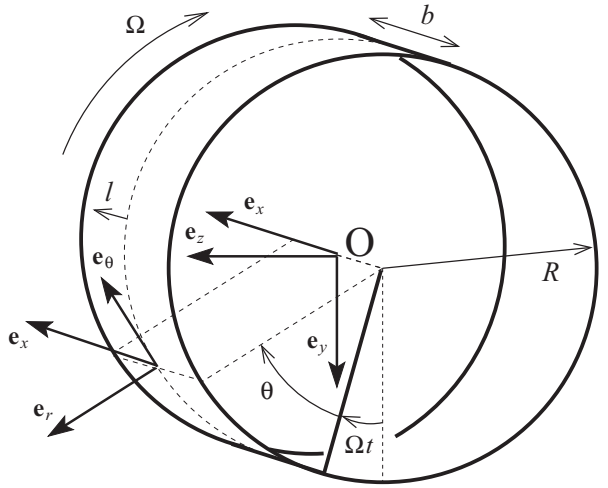


**Fig. 1.** The assumed undeformed belt geometry, consisting of a circular cylinder of radius $R$ and width $b$. A material point on the belt (rotating with angular velocity $\Omega$) is located by the coordinates $l$ and $\theta$.

at angle $\theta$ relative to a reference radius,

$$\mathbf{e}_r = \mathbf{e}_y\cos(\theta+\Omega t)+\mathbf{e}_z\sin(\theta+\Omega t), \tag{1}$$

$$\mathbf{e}_\theta = -\mathbf{e}_y\sin(\theta+\Omega t)+\mathbf{e}_z\cos(\theta+\Omega t), \tag{2}$$

where $\Omega$ is the angular velocity of the tyre. The belt itself is modelled as a surface of infinitesimal thickness, so the position vector of a material point before deformation is $\mathbf{r}^{(0)}(\theta,l,t)=R\mathbf{e}_r+l\mathbf{e}_x$, where $R$ is the cylinder radius and $l$ the local $x$ coordinate, measured relative to the belt centre. The belt width is $b$.

The belt deformation is specified by the vector $\mathbf{u}(\theta,l,t)=u(\theta,l,t)\mathbf{e}_x+v(\theta,l,t)\mathbf{e}_\theta+w(\theta,l,t)\mathbf{e}_r$. Sanders [13] gives the corresponding linear strain components as

$$\varepsilon_{11}=\frac{\partial u}{\partial l},\quad \varepsilon_{22}=\frac{1}{R}\frac{\partial v}{\partial\theta}+\frac{w}{R},\quad \varepsilon_{12}=\frac{\partial v}{\partial l}+\frac{1}{R}\frac{\partial u}{\partial\theta}, \tag{3}$$

and the curvatures as

$$\chi_1=-\frac{\partial^2 w}{\partial l^2},\quad \chi_2=-\frac{1}{R^2}\frac{\partial^2 w}{\partial\theta^2}+\frac{1}{R^2}\frac{\partial v}{\partial\theta},\quad \chi_{12}=-\frac{1}{R}\frac{\partial^2 w}{\partial\theta\partial l}+\frac{3}{4R}\frac{\partial v}{\partial l}-\frac{1}{4R^2}\frac{\partial u}{\partial\theta}. \tag{4}$$

(In these expressions, direction 1 corresponds to the coordinate $l$, and 2 to $\theta$.)

We shall also require second-order accurate expressions for the elongation in the $x$ and $\theta$ directions. Consider, first, an element of length $\delta l$ in the $x$ direction, with ends at $\mathbf{r}^{(0)}=R\mathbf{e}_r+l\mathbf{e}_x$ and $\mathbf{r}^{(0)}+\delta l\mathbf{e}_x$. After deformation, these lie at, respectively, $\mathbf{r}^{(0)}+\mathbf{u}$ and $\mathbf{r}^{(0)}+\delta l\mathbf{e}_x+\mathbf{u}+(\partial\mathbf{u}/\partial l)\delta l+O(\delta l^2)$. The new length of the element is thus

$$\delta l'=\delta l\sqrt{\left(1+\frac{\partial u}{\partial l}\right)^2+\left(\frac{\partial v}{\partial l}\right)^2+\left(\frac{\partial w}{\partial l}\right)^2}+O(\delta l^2) \tag{5}$$

and the strain is

$$e_{11}=\lim_{\delta l\to 0}\frac{\delta l'-\delta l}{\delta l}=\frac{\partial u}{\partial l}+\frac{1}{2}\left(\frac{\partial v}{\partial l}\right)^2+\frac{1}{2}\left(\frac{\partial w}{\partial l}\right)^2, \tag{6}$$

correct to quadratic order in the displacement derivatives. The corresponding expression for the azimuthal direction is

$$e_{22}=\frac{1}{R}\left(\frac{\partial v}{\partial\theta}+w\right)+\frac{1}{2R^2}\left(\frac{\partial u}{\partial\theta}\right)^2+\frac{1}{2R^2}\left(v-\frac{\partial w}{\partial\theta}\right)^2. \tag{7}$$

Finally, consider the volume swept by a surface element during the deformation (Fig. 2). The area of the element is initially $R\mathrm{d}\theta\,\mathrm{d}l$, and it undergoes a displacement $\mathbf{u}$. At a proportion $s$ of this displacement, the sides of the element are defined by the vectors $\mathbf{G}_\theta\,\mathrm{d}\theta$ and $\mathbf{G}_l\,\mathrm{d}l$, where

$$\mathbf{G}_\theta=\frac{\partial}{\partial\theta}(\mathbf{r}^{(0)}+s\mathbf{u})=s\frac{\partial u}{\partial\theta}\mathbf{e}_x+\left[R+s\frac{\partial v}{\partial\theta}+sw\right]\mathbf{e}_\theta-s\left(v-\frac{\partial w}{\partial\theta}\right)\mathbf{e}_r, \tag{8}$$

$$\mathbf{G}_l=\frac{\partial}{\partial l}(\mathbf{r}^{(0)}+s\mathbf{u})=\left(1+s\frac{\partial u}{\partial l}\right)\mathbf{e}_x+s\frac{\partial v}{\partial l}\mathbf{e}_\theta+s\frac{\partial w}{\partial l}\mathbf{e}_r. \tag{9}$$

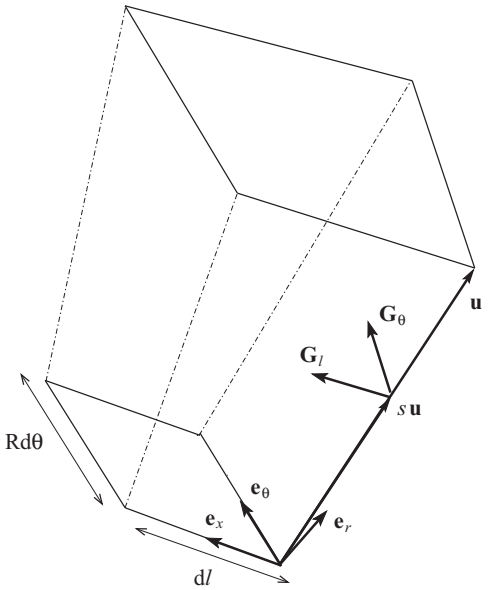


**Fig. 2.** The volume swept out by a belt element due to the deformation field **u**. The variable $s$ parameterises the deformation; at the intermediate stage $s\mathbf{u}$ the vectors $\mathbf{G}_l$ and $\mathbf{G}_\theta$ are parallel to the edges of the deformed element.

For an increment d$s$ in $s$, the volume swept out is $(\mathbf{G}_\theta \times \mathbf{G}_l)\cdot\mathbf{u}\,\mathrm{d}s\,\mathrm{d}\theta\,\mathrm{d}l$, and integrating from $s=0$ to 1 yields the result

$$\mathrm{d}V = \left\{-\frac{1}{2}R\frac{\partial w}{\partial l}u + \frac{1}{2}\left(v-\frac{\partial w}{\partial \theta}\right)v + \left[R\left(1+\frac{1}{2}\frac{\partial u}{\partial l}\right)+\frac{1}{2}\frac{\partial v}{\partial \theta}+\frac{1}{2}w\right]w\right\}\mathrm{d}l\,\mathrm{d}\theta, \tag{10}$$

again to quadratic order.

### 2.1.2. The kinetic energy

From Eqs. (1) and (2), we have $\partial\mathbf{e}_r/\partial t = \Omega\mathbf{e}_\theta$ and $\partial\mathbf{e}_\theta/\partial t = -\Omega\mathbf{e}_r$. Hence the velocity of the belt element with undeformed location $\mathbf{r}^{(0)}$ is

$$\mathbf{v} = \frac{\partial}{\partial t}(\mathbf{r}^{(0)}+\mathbf{u}) = \frac{\partial u}{\partial t}\mathbf{e}_x + \left[\frac{\partial v}{\partial t}+\Omega(R+w)\right]\mathbf{e}_\theta + \left[\frac{\partial w}{\partial t}-\Omega v\right]\mathbf{e}_r. \tag{11}$$

The kinetic energy of the belt is

$$T = \frac{M}{2}\int_S |\mathbf{v}|^2 R\,\mathrm{d}l\,\mathrm{d}\theta, \tag{12}$$

where $M$ is the belt mass per unit area, and $S$ represents the belt surface.

### 2.1.3. The potential energy

The potential energy, $U$, is the sum of three terms: $U = U_s + U_p + U_a$, in which $U_s$ is the standard expression for the strain energy of the deformed belt, $U_p$ is the additional contribution due to pre-stress, and $U_a$ is the air cavity component. For a linear, orthotropic belt material, subject to small strains, the first term is (from the relations in Chapter 15 of [9])

$$U_s = \frac{1}{2}\int_S (a_{11}\varepsilon_{11}^2 + a_{22}\varepsilon_{22}^2 + 2a_{12}\varepsilon_{11}\varepsilon_{22} + g_{12}\varepsilon_{12}^2 + b_{11}\chi_1^2 + b_{22}\chi_2^2 + 2b_{12}\chi_1\chi_2 + h_{12}\chi_{12}^2)R\,\mathrm{d}l\,\mathrm{d}\theta. \tag{13}$$

In the more familiar case of an isotropic material, with thickness $h$, Young's modulus $E$ and Poisson's ratio $v$, the extensional stiffness terms are given by

$$a_{11} = a_{22} = \frac{Eh}{1-v^2}, \quad a_{12} = va_{11}, \quad g_{12} = \frac{1-v}{2}a_{11}, \tag{14}$$

and the bending stiffnesses by

$$b_{11} = b_{22} = \frac{Eh^3}{12(1-v^2)}, \quad b_{12} = vb_{11}, \quad h_{12} = 2(1-v)b_{11}. \tag{15}$$

The pre-stress contribution arises because of the mean belt tensions, which we take to be $t_i$ (per unit axial distance) in the circumferential direction, and $s_i$ (per unit circumferential distance) in the axial direction. Hence,

$$U_p = \int_S (s_i e_{11} + t_i e_{22}) R \, \mathrm{d}l \, \mathrm{d}\theta, \tag{16}$$

and the quadratic expressions for $e_{11}$ and $e_{22}$, (6) and (7), thus provide $U_p$ to the same order in the strain components as $U_s$. (Note that Campanac et al. [7] use the 'Cauchy strain', $e_{22} + \frac{1}{2}e_{22}^2$ in place of $e_{22}$, but then subsequently discard the $t_i e_{22}^2$ term as negligible.)

The air cavity potential arises from the work done by the internal pressure as the belt deforms. In a fully coupled calculation, this pressure would itself be taken to be a function of the belt displacements, but here we shall assume the two can be decoupled; i.e. the influence of the cavity pressure on the belt motions is confined to contributions from its mean component, $p_i$. (The acoustic pressure contribution to the hub force can then be calculated in a post-processing stage. Support for this approach comes from the coupled calculations of Richards [14], whose tyre and cavity modes show little modification from their uncoupled counterparts.) The potential associated with the element of Fig. 2 is $-p_i \, \mathrm{d}V$ and, using Eq. (10), we obtain

$$U_a = -p_i \int_S \left\{ -\frac{1}{2} R \frac{\partial w}{\partial l} u + \frac{1}{2}\left(v - \frac{\partial w}{\partial \theta}\right) v + \left[ R\left(1 + \frac{1}{2}\frac{\partial u}{\partial l}\right) + \frac{1}{2}\frac{\partial v}{\partial \theta} + \frac{1}{2} w \right] w \right\} \mathrm{d}l \, \mathrm{d}\theta. \tag{17}$$

### 2.1.4. The variational analysis

According to pp. 242–243 in Vol. 1 of Ref. [15], the equations of motion of a conservative system can be derived from the principle that the (time) integral of the energy difference $T-U$ is stationary. The procedure is standard and is set out in detail for our problem in Ref. [16]. It yields

$$\left[ -M\frac{\partial^2}{\partial t^2} + \left(\frac{g_{12}}{R^2} + \frac{h_{12}}{16R^4} + \frac{t_i}{R^2}\right)\frac{\partial^2}{\partial \theta^2} + a_{11}\frac{\partial^2}{\partial l^2} \right] u + \left(\frac{a_{12}+g_{12}}{R} - \frac{3h_{12}}{16R^3}\right)\frac{\partial^2 v}{\partial l \partial \theta} + \left[ \frac{h_{12}}{4R^3}\frac{\partial^3}{\partial l \partial \theta^2} + \left(\frac{a_{12}}{R} - p_i\right)\frac{\partial}{\partial l} \right] w = -s_l, \tag{18}$$

$$\left(\frac{a_{12}+g_{12}}{R} - \frac{3h_{12}}{16R^3}\right)\frac{\partial^2 u}{\partial \theta \partial l} + \left[ -M\frac{\partial^2}{\partial t^2} + \left(\frac{a_{22}}{R^2} + \frac{b_{22}}{R^4}\right)\frac{\partial^2}{\partial \theta^2} + \left(g_{12} + \frac{9h_{12}}{16R^2} + s_i\right)\frac{\partial^2}{\partial l^2} \right] v + \left[ -2M\Omega\frac{\partial}{\partial t} - \frac{b_{22}}{R^4}\frac{\partial^3}{\partial \theta^3} - \frac{4b_{12}+3h_{12}}{4R^2}\frac{\partial^3}{\partial \theta \partial l^2} + \left(\frac{a_{22}}{R^2} + \frac{t_i}{R^2} - \frac{p_i}{R}\right)\frac{\partial}{\partial \theta} \right] w = -s_\theta, \tag{19}$$

$$-\left[ \frac{h_{12}}{4R^3}\frac{\partial^3}{\partial l \partial \theta^2} + \left(\frac{a_{12}}{R} - p_i\right)\frac{\partial}{\partial l} \right] u + \left[ 2M\Omega\frac{\partial}{\partial t} + \frac{b_{22}}{R^4}\frac{\partial^3}{\partial \theta^3} - \left(\frac{a_{22}}{R^2} + \frac{t_i}{R^2} - \frac{p_i}{R}\right)\frac{\partial}{\partial \theta} + \frac{4b_{12}+3h_{12}}{4R^2}\frac{\partial^3}{\partial \theta \partial l^2} \right] v + \left[ -M\frac{\partial^2}{\partial t^2} - \frac{b_{22}}{R^4}\frac{\partial^4}{\partial \theta^4} - \frac{2b_{12}+h_{12}}{R^2}\frac{\partial^4}{\partial \theta^2 \partial l^2} - b_{11}\frac{\partial^4}{\partial l^4} + \frac{t_i}{R^2}\frac{\partial^2}{\partial \theta^2} + s_i\frac{\partial^2}{\partial l^2} - \left(\frac{a_{22}}{R^2} - \frac{p_i}{R} - M\Omega^2\right) \right] w = -s_r \tag{20}$$

for applied force densities $s_l, s_\theta$ and $s_r$ in the axial, circumferential and radial directions. We also obtain the auxiliary relation $t_i = p_i R + M\Omega^2 R^2$, and the boundary stress resultants

$$f_u = a_{11}\frac{\partial u}{\partial l} + \frac{a_{12}}{R}\frac{\partial v}{\partial \theta} + \left(\frac{a_{12}}{R} - \frac{p_i}{2}\right) w + s_i, \tag{21}$$

$$f_v = \left(\frac{g_{12}}{R} - \frac{3h_{12}}{16R^3}\right)\frac{\partial u}{\partial \theta} + \left(g_{12} + \frac{9h_{12}}{16R^2} + s_i\right)\frac{\partial v}{\partial l} - \frac{3h_{12}}{4R^2}\frac{\partial^2 w}{\partial \theta \partial l}, \tag{22}$$

$$f_w = \left( -\frac{h_{12}}{4R^3}\frac{\partial^2}{\partial \theta^2} + \frac{p_i}{2} \right) u + \frac{4b_{12}+3h_{12}}{4R^2}\frac{\partial^2 v}{\partial l \partial \theta} - \left( b_{11}\frac{\partial^3}{\partial l^3} + \frac{b_{12}+h_{12}}{R^2}\frac{\partial^3}{\partial l \partial \theta^2} - s_i\frac{\partial}{\partial l} \right) w, \tag{23}$$

$$r_w = -\frac{b_{12}}{R^2}\frac{\partial v}{\partial \theta} + \left( \frac{b_{12}}{R^2}\frac{\partial^2}{\partial \theta^2} + b_{11}\frac{\partial^2}{\partial l^2} \right) w. \tag{24}$$

The sign conventions applicable here are shown in Fig. 3.

### 2.1.5. Comparison with prior formulations

Our analysis can be viewed as a generalisation of Campanac et al.'s variational derivation for a belt of negligible width [7]. Thus, one would expect Eqs. (19) and (20) to reduce to their expressions if axial derivatives and terms in $u$ are removed. There are, however, some discrepancies, even after accounting for the difference in reference frame (which is not rotating in Ref. [7]). Specifically, the terms in $p_i/R$ multiplying $\partial w/\partial \theta$ in Eq. (19), and $\partial v/\partial \theta$ and $\partial^2 w/\partial \theta^2$ in Eq. (20), are absent in [7], because quadratic order terms in the air cavity potential have been omitted. This omission also augments Eq. (19) with a term in $v$. In our application the difference to the equations is numerically trivial, but the additional contribution

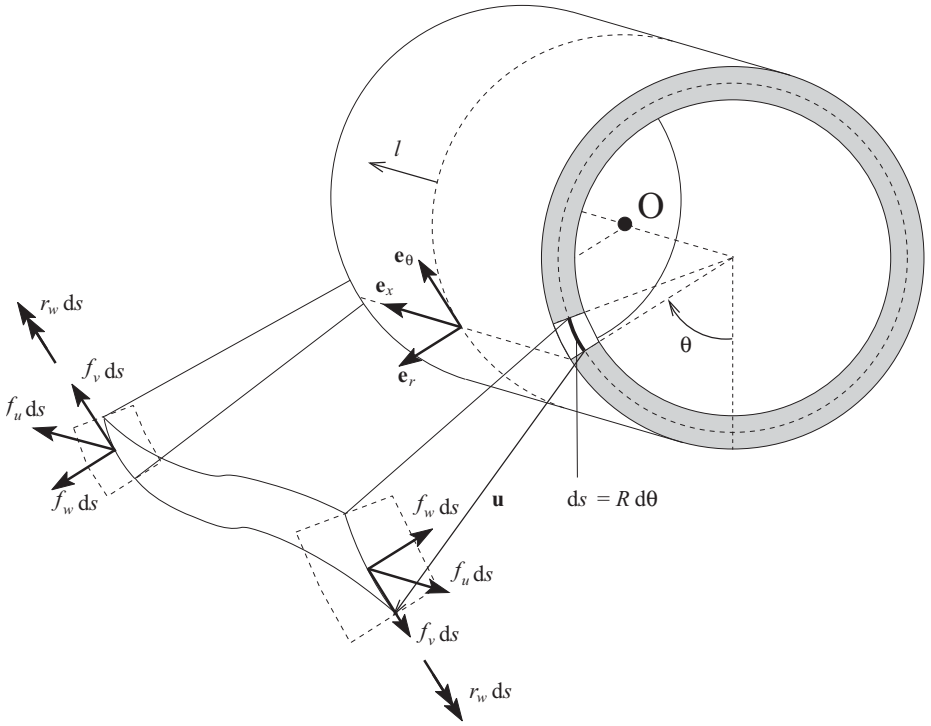


**Fig. 3.** Nomenclature and sign conventions for the forces ($f_u, f_v, f_w$) and moments ($r_w$) acting at the belt edges.

proportional to $v$ in Eq. (19) leads to Campanac et al. predicting an unphysical restoring force when the belt undergoes a rigid-body azimuthal rotation.

On substituting the isotropic forms, (14) and (15), for the elastic constants, we can also compare our equations with those of Kim and Bolton [8]. Here a number of differences are apparent. Most of these can be traced back to conflicts in the strain expressions presented by Sanders [13] and Soedel [9] (Kim and Bolton's source). Such discrepancies are a feature of alternative shell theories, and usually have insignificant accuracy implications in practice. Note, however, that the coefficient symmetry evident in Eqs. (18)–(20) is not present in the Soedel formulation. Also, calculations using the isotropic forms of (18)–(20) have been compared with a number of established shell theories [17], and have shown excellent agreement. Finally, there are additional differences in the pre-stress and pressurisation terms, as Kim and Bolton only consider their contributions in the radial direction. These, too, are expected to be negligible (for example, the factor $(t_i - p_i R)/R^2$ multiplying $\partial v/\partial\theta$ in (20) is absent from Kim and Bolton's formulation, but for typical parameter values it is dwarfed by the other coefficient of $\partial v/\partial\theta$, $a_{22}/R^2$).

A similarly detailed comparison with Pinnington's belt equations [10] is not possible, due to the more fundamental differences in his formulation. Some general observations can, however, be made. Pinnington only gives circumferential and radial equations and, in these, there are no terms in the axial displacement, $u$. Derivatives of $v$ in his equivalent of (19) appear at the same order; likewise those of $w$ in (20). The coupling terms, however, involve derivatives at different orders, for reasons that are not immediately obvious.

Finally, our expressions for the boundary stress resultants, (21)–(24), do not appear to have been given before. They are, however, essential to a rigorous treatment of the coupling between the belt and the sidewalls.

### 2.1.6. *The unforced solutions*

Our ultimate aim is to find the impulse response of the belt. Since this implies localised forcing, it will be expressible elsewhere in terms of the solutions to Eqs. (18)–(20) when $s_r = s_\theta = s_l = 0$.

The first step is to take a double Fourier transform. We define

$$\hat{u}(n,l,\omega) = \int_{-\infty}^{\infty}\int_{-\pi}^{\pi} u(\theta,l,t)\mathrm{e}^{-\mathrm{i}n\theta}\mathrm{e}^{-\mathrm{i}\omega t}\,\mathrm{d}\theta\,\mathrm{d}t \tag{25}$$

and $\hat{v}(n,l,\omega)$, $\hat{w}(n,l,\omega)$ similarly. Then the Fourier transform of (18)–(20) can be expressed in a canonical form suitable for numerical analysis, viz.

$$\mathbf{A}\hat{\mathbf{g}} + \mathbf{B}\frac{\mathrm{d}\hat{\mathbf{g}}}{\mathrm{d}l} = \mathbf{0}, \tag{26}$$

where

$$\hat{\mathbf{g}} = \left[\hat{u} \;\; \frac{\mathrm{d}\hat{u}}{\mathrm{d}l} \;\; \hat{v} \;\; \frac{\mathrm{d}\hat{v}}{\mathrm{d}l} \;\; \hat{w} \;\; \frac{\mathrm{d}\hat{w}}{\mathrm{d}l} \;\; \frac{\mathrm{d}^2\hat{w}}{\mathrm{d}l^2} \;\; \frac{\mathrm{d}^3 w}{\mathrm{d}l^3}\right]^{\mathrm{T}} \tag{27}$$

and

$$\mathbf{A} = \begin{bmatrix} A_{11} & 0 & 0 & A_{14} & 0 & A_{16} & 0 & 0 \\ 0 & 1 & 0 & 0 & 0 & 0 & 0 & 0 \\ 0 & A_{14} & A_{33} & 0 & A_{35} & 0 & A_{37} & 0 \\ 0 & 0 & 0 & 1 & 0 & 0 & 0 & 0 \\ 0 & -A_{16} & -A_{35} & 0 & A_{55} & 0 & A_{57} & 0 \\ 0 & 0 & 0 & 0 & 0 & 1 & 0 & 0 \\ 0 & 0 & 0 & 0 & 0 & 0 & 1 & 0 \\ 0 & 0 & 0 & 0 & 0 & 0 & 0 & 1 \end{bmatrix}, \tag{28}$$

with

$$A_{11} = M\omega^2 - \frac{n^2}{R^2}\left(g_{12} + \frac{h_{12}}{16R^2} + t_i\right), \quad A_{14} = \frac{\mathrm{i}n}{R}\left(a_{12} + g_{12} - \frac{3h_{12}}{16R^2}\right), \tag{29}$$

$$A_{16} = \frac{a_{12}}{R} - p_i - n^2\frac{h_{12}}{4R^3}, \quad A_{33} = M\omega^2 - \frac{n^2}{R^2}\left(a_{22} + \frac{b_{22}}{R^2}\right), \tag{30}$$

$$A_{35} = -2\mathrm{i}M\Omega\omega + \frac{\mathrm{i}n}{R^2}(a_{22} + t_i - p_i R) + \frac{\mathrm{i}n^3}{R^4}b_{22}, \quad A_{37} = -\frac{\mathrm{i}n}{R^2}\left(b_{12} + \frac{3h_{12}}{4}\right), \tag{31}$$

$$A_{55} = M\omega^2 - \frac{a_{22}}{R^2} + \frac{p_i}{R} + M\Omega^2 - \frac{n^2}{R^2}t_i - \frac{n^4}{R^4}b_{22}, \quad A_{57} = \frac{n^2}{R^2}(2b_{12} + h_{12}) + s_i; \tag{32}$$

$$\mathbf{B} = \begin{bmatrix} 0 & a_{11} & 0 & 0 & 0 & 0 & 0 & 0 \\ -1 & 0 & 0 & 0 & 0 & 0 & 0 & 0 \\ 0 & 0 & 0 & g_{12} + \dfrac{9h_{12}}{16R^2} + s_i & 0 & 0 & 0 & 0 \\ 0 & 0 & -1 & 0 & 0 & 0 & 0 & 0 \\ 0 & 0 & 0 & \mathrm{i}n\dfrac{4b_{12} + 3h_{12}}{4R^2} & 0 & 0 & 0 & -b_{11} \\ 0 & 0 & 0 & 0 & -1 & 0 & 0 & 0 \\ 0 & 0 & 0 & 0 & 0 & -1 & 0 & 0 \\ 0 & 0 & 0 & 0 & 0 & 0 & -1 & 0 \end{bmatrix}. \tag{33}$$

The next step is to express $\hat{\mathbf{g}}$ in terms of the eigenvectors of $\mathbf{A}$ and $\mathbf{B}$. These are the vectors $\boldsymbol{\phi}_j$ that satisfy

$$(\mathbf{A} - \lambda_j\mathbf{B})\boldsymbol{\phi}_j = \mathbf{0}. \tag{34}$$

There are eight such vectors, and each has an associated, unique eigenvalue $\lambda_j$. We write

$$\hat{\mathbf{g}} = \sum_{j=1}^{8} y_j\boldsymbol{\phi}_j \tag{35}$$

and substitute this expression into (26). Since each eigenvector obeys (34), we obtain

$$\sum_{j=1}^{8}\left(\lambda_j y_j + \frac{\mathrm{d}y_j}{\mathrm{d}l}\right)\mathbf{B}\boldsymbol{\phi}_j = \mathbf{0}. \tag{36}$$

Now, as long as the vectors $\mathbf{B}\boldsymbol{\phi}_j$ are independent, this implies that

$$\lambda_j y_j + \frac{\mathrm{d}y_j}{\mathrm{d}l} = 0 \tag{37}$$

for each $j$, i.e.

$$y_j = c_j\mathrm{e}^{-\lambda_j l}, \tag{38}$$

where the $c_j$s are unknown constants. They are determined by the applicable boundary conditions which, in our case, depend on the sidewall. Their evaluation is thus considered after the description of the sidewall model.

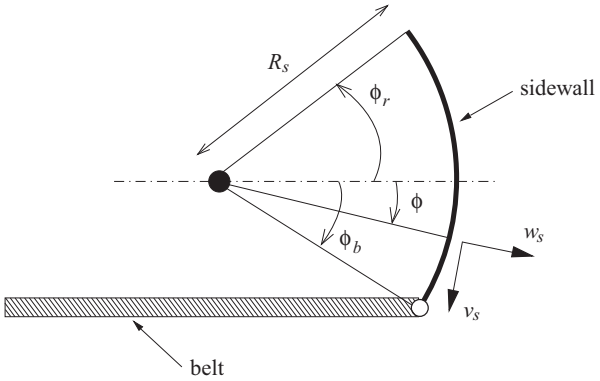


**Fig. 4.** The assumed undeformed sidewall geometry, a circular arc of radius $R_s$. Positions on the sidewall are located by the angle $\phi$. The displacement components are $v_s$ and $w_s$.

### 2.2. The sidewall model

In principle, the tyre sidewall can be analysed similarly to the belt. Such an approach would, however, lead to a set of equations of motion with variable, rather than constant, coefficients. This feature arises because the sidewalls, fully modelled, differ from the belt in two ways: they have curvature about two axes and they experience a spatially varying centripetal acceleration. There are, however, good reasons to neglect these aspects. First, the secondary curvature is small, and the sidewall is (as will be seen later) rather compliant in the circumferential direction, suggesting that a one-dimensional representation, neglecting circumferential variations, may be sufficient. Second, the non-uniform tension and Coriolis acceleration due to the varying radial position are likely to be small, due (respectively) to the dominance of internal pressurisation and the low sidewall mass in comparison to the belt. (Also, a previous study of the importance of the Coriolis terms in the belt context [17] concluded that they have little influence.) We therefore model the sidewall as a distribution of radial elements, decoupled in the circumferential direction. Additionally, as the thickness is small compared to the belt (at least for conventional tyres), we neglect bending stiffness.

This sidewall representation differs from Pinnington's [11] in two important respects. First, it does not support bending or shear waves, which become important at frequencies above our region of interest [11,18]. Second, we have not adopted Pinnington's heuristic method for handling the sidewall response to circumferentially varying forcing. This approach implies an isotropic dispersion relation, which cannot easily be justified, especially at frequencies where the restoring forces are dominated by the membrane tension contribution (which is vastly greater in the radial direction). We therefore claim that the neglect of circumferential stiffness is preferable at this stage. (We return to this issue when we consider how to link the belt and sidewall formulations, in Section 2.3.2.)

#### 2.2.1. Sidewall governing equations

In the absence of bending stiffness and inertia forces due to centripetal acceleration, the pressurised sidewall takes up a circular arc shape (Fig. 4). The radius of this arc is taken to be $R_s$, and material points along it are specified by the angle $\phi$. The rim end of the sidewall is at $\phi=-\phi_r$, and the belt end at $\phi=\phi_b$. Perturbations from this undeformed state are characterised by the azimuthal and radial components $v_s$ and $w_s$.

The equations of motion for this representation follow straightforwardly from a variational analysis based on the simplified equivalents of Eqs. (12), (11), (13), (3), (16), (7) and (17). We obtain

$$\left[-M_s\frac{\partial^2}{\partial t^2}+\frac{a_s}{R_s^2}\frac{\partial^2}{\partial\phi^2}\right]v_s+\frac{a_s}{R_s^2}\frac{\partial w_s}{\partial\phi}=0, \tag{39}$$

$$-\frac{a_s}{R_s^2}\frac{\partial v_s}{\partial\phi}+\left[-M_s\frac{\partial^2}{\partial t^2}+\frac{t_s}{R_s^2}\frac{\partial^2}{\partial\phi^2}-\frac{a_s}{R_s^2}+\frac{p_i}{R_s}\right]w_s=0, \tag{40}$$

with the supplementary condition that $t_s=p_iR_s$. The boundary forces (Fig. 5) are given by

$$f_{vs}=\frac{a_s}{R_s}\left(\frac{\partial v_s}{\partial\phi}+w_s\right)+t_s-p_i\frac{w_s}{2}, \tag{41}$$

$$f_{ws}=\frac{t_s}{R_s}\left(\frac{\partial w_s}{\partial\phi}-v_s\right)+p_i\frac{v_s}{2}. \tag{42}$$

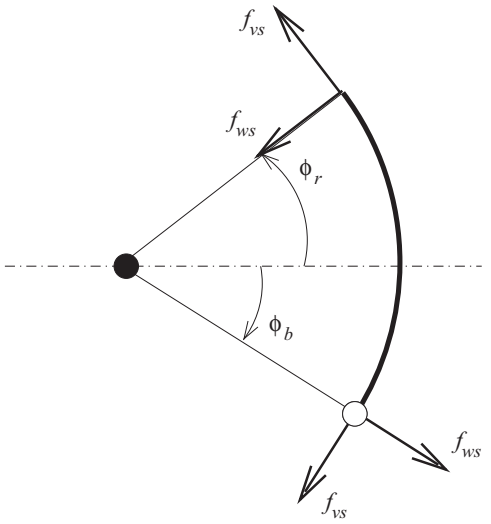


**Fig. 5.** Nomenclature and sign conventions for the forces acting at the ends of the sidewall.

*2.2.2. The sidewall static stiffness*

At low enough frequencies, the sidewalls will present a spring-like impedance to the belt edges. Analytical expressions for its components follow from the steady solutions of Eqs. (39) and (40), with $v_s = w_s = 0$ at the rim junction ($\phi = -\phi_r$). As the purpose of these solutions is to provide insight, we make the further assumption of a symmetric sidewall, i.e. $\phi_r = \phi_b = \phi_s$. The steady displacements satisfying (39), (40) and the rim boundary condition are then

$$v_s = v_0[1-\cos(\phi+\phi_s)] + w_0\sin(\phi+\phi_s) - w_0\left(1-\frac{p_i R_s}{a_s}\right)(\phi+\phi_s), \tag{43}$$

$$w_s = w_0[1-\cos(\phi+\phi_s)] - v_0\sin(\phi+\phi_s), \tag{44}$$

where $v_0$ and $w_0$ are unknown constants.

We now consider a constrained vertical displacement of the belt junction, by a distance $\delta$, i.e. $v_s = \delta\cos\phi_s, w_s = \delta\sin\phi_s$. In this case, we have

$$v_0 = \frac{\delta}{2}\frac{\left(1-\frac{p_i R_s}{a_s}\right)\phi_s}{\sin\phi_s - \left(1-\frac{p_i R_s}{a_s}\right)\phi_s\cos\phi_s}, \tag{45}$$

$$w_0 = \frac{\delta}{2}\frac{1}{\sin\phi_s - \left(1-\frac{p_i R_s}{a_s}\right)\phi_s\cos\phi_s}. \tag{46}$$

The perturbation force in the same direction, $F$, is $(f_{vs}-t_s)\cos\phi_s + f_{ws}\sin\phi_s$ and, using Eqs. (41)–(46), we find the stiffness

$$\frac{F}{\delta} = \frac{p_i}{2}\frac{\cos\phi_s + \left(1-\frac{p_i R_s}{a_s}\right)\phi_s\sin\phi_s}{\sin\phi_s - \left(1-\frac{p_i R_s}{a_s}\right)\phi_s\cos\phi_s}. \tag{47}$$

This expression represents a generalisation of the inextensible ($a_s \to \infty$) result derived by Pinnington [18]. The modifying factor $(1-p_i R_s/a_s)$ will be very close to one (since $p_i R_s/a_s = t_s/a_s$ is the mean sidewall strain, which must be small by design), but its presence in the denominator is potentially important nonetheless, because the terms $\sin\phi_s$ and $\phi_s\cos\phi_s$ (almost) cancel for small $\phi_s$, leaving a significant relative contribution from $(p_i R_s/a_s)\phi_s\cos\phi_s$. The inextensible result is thus useful for indicative purposes, without being totally reliable.

If, instead, we consider the horizontal force associated with a displacement constrained to be in the horizontal direction, i.e. with $v_s = -\delta\sin\phi_s$, $w_s = \delta\cos\phi_s$ and $F = -(f_{vs}-t_s)\sin\phi_s + f_{ws}\cos\phi_s$, then the constants in (43) and (44) are given by $v_0 = -\delta/2\sin\phi_s, w_0 = 0$, so the stiffness is

$$\frac{F}{\delta} = \frac{p_i}{2}\frac{\cos\phi_s}{\sin\phi_s}. \tag{48}$$

For the representative values $p_i = 2.2 \times 10^5$ Pa, $\phi_s = 30^\circ$, this is $1.9 \times 10^5$ Pa. The corresponding radial stiffness (with $p_i R_s/a_s$ neglected) is $2.7 \times 10^6$ Pa. Thus, at least for low frequencies, we expect the sidewall's radial impedance to dominate.

*2.2.3. General solution of the sidewall equations*

For non-zero frequencies, the solution of Eqs. (39) and (40) can be obtained in a similar way to that for the belt. The Fourier-transformed variables are now $\hat{v}_s(n,\phi,\omega)$ and $\hat{w}_s(n,\phi,\omega)$, where the dependence on tyre azimuthal angle implied by $n$ is introduced in anticipation of linking the belt and sidewall representations. The equations of motion become

$$\mathbf{A}_s\hat{\mathbf{g}}_s + \mathbf{B}_s\frac{\mathrm{d}\hat{\mathbf{g}}_s}{\mathrm{d}\phi} = \mathbf{0}, \tag{49}$$

where

$$\hat{\mathbf{g}}_s = \left[\hat{v}_s \;\; \frac{\mathrm{d}\hat{v}_s}{\mathrm{d}\phi} \;\; \hat{w}_s \;\; \frac{\mathrm{d}\hat{w}_s}{\mathrm{d}\phi}\right]^{\mathrm{T}}, \tag{50}$$

$$\mathbf{A}_s = \begin{bmatrix} M_s\omega^2 & 0 & 0 & \dfrac{a_s}{R_s^2} \\ 0 & 1 & 0 & 0 \\ 0 & -\dfrac{a_s}{R_s^2} & M_s\omega^2 - \dfrac{a_s}{R_s^2} + \dfrac{p_i}{R_s} & 0 \\ 0 & 0 & 0 & 1 \end{bmatrix}, \quad \mathbf{B}_s = \begin{bmatrix} 0 & \dfrac{a_s}{R_s^2} & 0 & 0 \\ -1 & 0 & 0 & 0 \\ 0 & 0 & 0 & \dfrac{t_s}{R_s^2} \\ 0 & 0 & -1 & 0 \end{bmatrix}. \tag{51}$$

The eigenvalues, $\mu_j$, and eigenvectors, $\boldsymbol{\psi}_j$, of $\mathbf{A}_s$ and $\mathbf{B}_s$ satisfy $(\mathbf{A}_s - \mu_j\mathbf{B}_s)\boldsymbol{\psi}_j = \mathbf{0}$, and we again expand the vector of unknowns in terms of the eigenvectors:

$$\hat{\mathbf{g}}_s = \sum_{j=1}^{4} z_j\boldsymbol{\psi}_j. \tag{52}$$

The same substitutions and manipulations as previously then yield the result that

$$z_j = d_j\mathrm{e}^{-\mu_j\phi} \tag{53}$$

with the unknown constants $d_j$ to be determined by the boundary conditions.

*2.3. The response to an impulsive force*

Although the ultimate aim of this model is to provide the response of the force at the wheel hub to an impulse at the belt, the corresponding belt response is also of interest, particularly for validation purposes. Here we show how the previous results may be coupled to provide this information.

*2.3.1. The general solution to impulsive forcing*

Without loss of generality, we can take the impulse to be applied at $\theta = 0$ and $l = l_d$. Away from this point, the solution obeys the unforced equations considered in Section 2.1.6. It can thus be similarly expressed as a superposition of Fourier components, specifically:

$$\hat{\mathbf{g}}^- = \boldsymbol{\Phi}\mathrm{e}^{-\boldsymbol{\Lambda}l}\mathbf{c}^-, \quad l < l_d, \tag{54}$$

$$\hat{\mathbf{g}}^+ = \boldsymbol{\Phi}\mathrm{e}^{-\boldsymbol{\Lambda}l}\mathbf{c}^+, \quad l > l_d. \tag{55}$$

These expressions are the matrix–vector equivalents of Eqs. (35) and (38) combined. The column vectors $\mathbf{c}^+, \mathbf{c}^-$ contain the unknown coefficients; $\boldsymbol{\Phi} = [\boldsymbol{\phi}_1 \;\; \boldsymbol{\phi}_2 \;\; \ldots \;\; \boldsymbol{\phi}_8]$ is the eigenvector matrix and $\boldsymbol{\Lambda}$ is the diagonal matrix whose entries are the eigenvalues. The coefficient sets $c_j^-$ and $c_j^+$ differ due to the impulse at $l = l_d$, but are not fully independent of one another; they are related by integrating the equations of motion across the impulse location.

First, we specify the impulse explicitly, i.e. one of the surface stresses (depending on the impulse direction) is taken equal to $R^{-1}\delta(\theta)\delta(l-l_d)\delta(t)$, where $\delta()$ is the Dirac delta function. On now Fourier transforming Eqs. (18)–(21) as before, we have

$$\mathbf{A}\hat{\mathbf{g}} + \mathbf{B}\frac{\mathrm{d}\hat{\mathbf{g}}}{\mathrm{d}l} = -\frac{\mathbf{e}_k}{R}\delta(l-l_d), \tag{56}$$

where $\mathbf{e}_k$ is the $k$-th unit vector (e.g. $\mathbf{e}_1 = [1\;0\;0\;0\;0\;0\;0\;0]^{\mathrm{T}}$) and $k$ can take the values 1, 3 or 5, for axial, azimuthal or radial impulses, respectively. The form of this equation implies that $\hat{\mathbf{g}}$ can contain discontinuities, but no singularities, so integrating it over the infinitesimal interval either side of $l = l_d$ gives

$$\mathbf{B}\boldsymbol{\Phi}\mathrm{e}^{-\boldsymbol{\Lambda}l_d}(\mathbf{c}^+ - \mathbf{c}^-) = -\frac{\mathbf{e}_k}{R}. \tag{57}$$

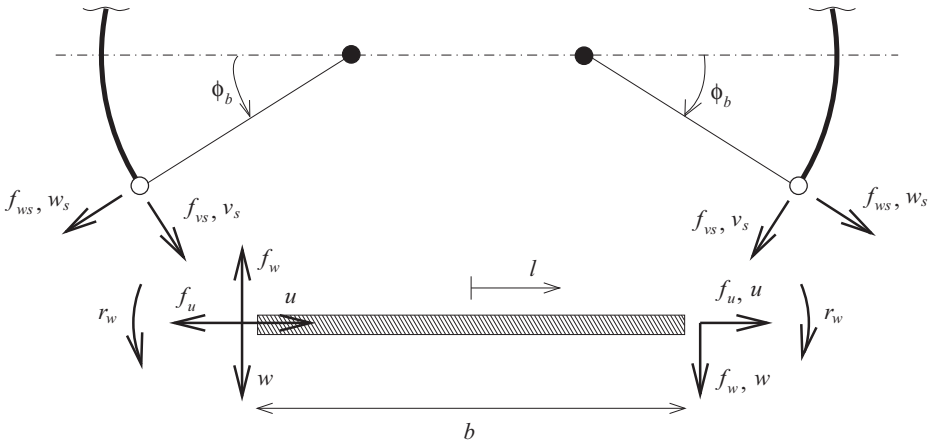


**Fig. 6.** Exploded view of belt/sidewall junction.

This represents eight linear equations in the 16 unknown elements of $\mathbf{c}^+$, $\mathbf{c}^-$. The additional relations that we require must be found from the belt boundary conditions.

*2.3.2. Coupling the belt and sidewalls*

The belt boundary conditions are determined by the sidewall dynamics, so that additional unknowns as well as additional conditions will be introduced. For the sidewall joining the tyre at $l=+b/2$, we write the Fourier-transformed response vector as

$$\hat{\mathbf{g}}_s^+ = \mathbf{\Psi} e^{-\mathbf{M}\phi}\mathbf{d}^+, \tag{58}$$

where $\mathbf{\Psi}$ and $\mathbf{M}$ are, respectively, the sidewall eigenvector and eigenvalue matrices. The expression for the response vector on the other side of the belt ($l=-b/2$) takes the same form, but with Fourier components

$$\hat{\mathbf{g}}_s^- = \mathbf{\Psi} e^{-\mathbf{M}\phi}\mathbf{d}^-. \tag{59}$$

Fig. 6 shows an exploded view of the combined belt/sidewalls geometry. The conditions we wish to impose at the junctions are continuity of displacement, force and moment. We also need to specify the circumferential boundary force, which is not provided by our model.

Continuity of displacements gives

$$-v_s\sin\phi_b + w_s\cos\phi_b = \pm u, \tag{60}$$

$$v_s\cos\phi_b + w_s\sin\phi_b = w, \tag{61}$$

where the alternative signs apply for $l=\pm b/2$, respectively. After Fourier transformation, these equations can be expressed in the matrix form:

$$\begin{bmatrix} -\sin\phi_b & 0 & \cos\phi_b & 0 \\ \cos\phi_b & 0 & \sin\phi_b & 0 \end{bmatrix}\hat{\mathbf{g}}_s^{\pm} = \begin{bmatrix} \pm\mathbf{e}_1^{\mathrm{T}} \\ \mathbf{e}_5^{\mathrm{T}} \end{bmatrix}\hat{\mathbf{g}}^{\pm}, \quad \phi=\phi_b, \quad l=\pm b/2. \tag{62}$$

Continuity of the perturbation forces implies that

$$-(f_{vs}-p_iR_s)\sin\phi_b + f_{ws}\cos\phi_b + (f_u - s_i) = 0, \tag{63}$$

$$(f_{vs}-p_iR_s)\cos\phi_b + f_{ws}\sin\phi_b \pm f_w = 0, \tag{64}$$

with the sign of the final term depending on whether $l=+b/2$ or $-b/2$. (The issue of steady force continuity is deferred until Section 4.) On using Eqs. (21), (23), (41), (42) and Fourier transforming, the resulting conditions are

$$\begin{bmatrix} -\sin\phi_b & \cos\phi_b \\ \cos\phi_b & \sin\phi_b \end{bmatrix}\begin{bmatrix} 0 & \frac{a_s}{R_s} & \frac{a_s}{R_s}-\frac{p_i}{2} & 0 \\ -\frac{t_s}{R_s}+\frac{p_i}{2} & 0 & 0 & \frac{t_s}{R_s} \end{bmatrix}\hat{\mathbf{g}}_s^{\pm} + \begin{bmatrix} \mathbf{F}_u \\ \pm\mathbf{F}_w \end{bmatrix}\hat{\mathbf{g}}^{\pm} = \mathbf{0}, \quad \phi=\phi_b, \quad l=\pm b/2, \tag{65}$$

where

$$\mathbf{F}_u = \left[0 \;\; a_{11} \;\; in\frac{a_{12}}{R} \;\; 0 \;\; \frac{a_{12}}{R}-\frac{p_i}{2} \;\; 0 \;\; 0 \;\; 0\right], \tag{66}$$

$$\mathbf{F}_w = \left[ n^2 \frac{h_{12}}{4R^3} + \frac{p_i}{2} \;\; 0 \;\; 0 \;\; \mathrm{i}n\frac{4b_{12}+3h_{12}}{4R^2} \;\; 0 \;\; n^2\frac{b_{12}+h_{12}}{R^2} + s_i \;\; 0 \;\; -b_{11} \right]. \tag{67}$$

For the circumferential boundary forces, we represent the (unmodelled) sidewall stiffness by a spring constant, $k_\theta$, i.e.

$$f_v = \mp k_\theta v, \tag{68}$$

where the opposing signs again refer to $l = +b/2$ and $-b/2$, respectively. The force component is given by Eq. (22), and the Fourier-transformed conditions are

$$\left[ \mathrm{i}n\left(\frac{g_{12}}{R} - \frac{3h_{12}}{16R^3}\right) \;\; 0 \;\; \pm k_\theta \;\; g_{12} + \frac{9h_{12}}{16R^2} + s_i \;\; 0 \;\; -\mathrm{i}n\frac{3h_{12}}{4R^2} \;\; 0 \;\; 0 \right] \hat{\mathbf{g}}^{\pm} = \mathbf{0}, \quad l = \pm b/2. \tag{69}$$

Finally, the sidewall carries no bending moment, so the moment resultant $r_w$ is zero on both sides of the belt. This leads, via Eq. (24) and the usual Fourier transformation, to

$$\left[ 0 \;\; 0 \;\; -\mathrm{i}n\frac{b_{12}}{R^2} \;\; 0 \;\; -n^2\frac{b_{12}}{R^2} \;\; 0 \;\; b_{11} \;\; 0 \right] \mathbf{\Phi} \mathrm{e}^{\mp \mathbf{\Lambda} b/2} \mathbf{c}^{\pm} = \mathbf{0}. \tag{70}$$

*2.3.3. The rim condition*

We assume that the wheel rim is effectively rigid as far as the belt and sidewall vibrations are concerned, i.e. $v_s = w_s = 0$ for $\phi = -\phi_r$. This implies

$$\begin{bmatrix} 1 & 0 & 0 & 0 \\ 0 & 0 & 1 & 0 \end{bmatrix} \mathbf{g}_s^{\pm} = \mathbf{0}, \quad \phi = -\phi_r. \tag{71}$$

*2.3.4. Solution for the impulse response*

Taken together, Eqs. (57), (62), (65) and (69)–(71) give 24 conditions on the 24 unknowns contained in $\mathbf{c}^-$, $\mathbf{c}^+$, $\mathbf{d}^-$ and $\mathbf{d}^+$. The resulting matrix equation is straightforward to solve for the coefficient vectors, and hence the Fourier-transformed response. The impulse response is then obtainable from the inverse Fourier transform in time and azimuthal angle.

## 3. Tyre measurements

The model presented in the previous section makes the assumption that the belt and sidewalls can legitimately be represented by simplified theoretical forms, whose defining parameters must be supplied. The purpose of the measurements described here was thus twofold: to investigate the fidelity of the model and to find appropriate values of the unknown elastic parameters. Since these are independent of rotation effects, and apply to displacements about an inflated, but unloaded, state, the experiments were carried out on a pressurised, stationary tyre. The following sections describe the apparatus used, the experimental method and the subsequent data analysis. Finally, some sample results are presented.

### *3.1. Apparatus*

The test tyre was a Goodyear 'Wrangler' 235/65/R17. It was mounted horizontally on a fixed, solid hub. Vibration excitation was provided by a Ling Dynamic Systems electro-dynamic shaker, model V101. For excitation in the radial direction, the shaker was attached to the tyre via a 15 mm diameter brass button glued to the tread rubber. Tangential (i.e. axial or azimuthal) excitation was applied through a push-rod with an end plate, the latter again being glued to the tread. The input level was determined using a Bruel and Kjaer force transducer, type 8200.

The tyre response in the radial direction was measured with a Polytec Laser Doppler Vibrometer. At some locations, the response in all three translational directions was found, using an Endevco ISOTRON tri-axial accelerometer, model 35A. All data were logged on an LMS SCADAS III system, connected to an HP-UX workstation.

### *3.2. Experimental method*

To ensure that the tyre was representative of an in-service example, it was first 'run in' for approximately 320 km at driving speeds in the range 50–110 km/h. (Note, however, that sample measurements taken before this process showed no significant differences from the main data set.) The inflation pressure was, in general, set to its nominal value: 2.2 bar; some measurements were also performed at higher and lower pressures. The temperature was ambient in all cases.

The shaker was driven with white noise, band-limited to 6400 Hz. The signals were anti-alias filtered to ensure cut-off by 4096 Hz, and logged at a sampling rate of 8192 Hz, for 20 s.

Radial response measurements were made around half the tyre circumference from the forcing location, at 5° intervals, and at five axial locations. The latter consisted of the belt centre, 3 cm either side and 6 cm either side. Tri-axial responses were taken over a subset of these points.

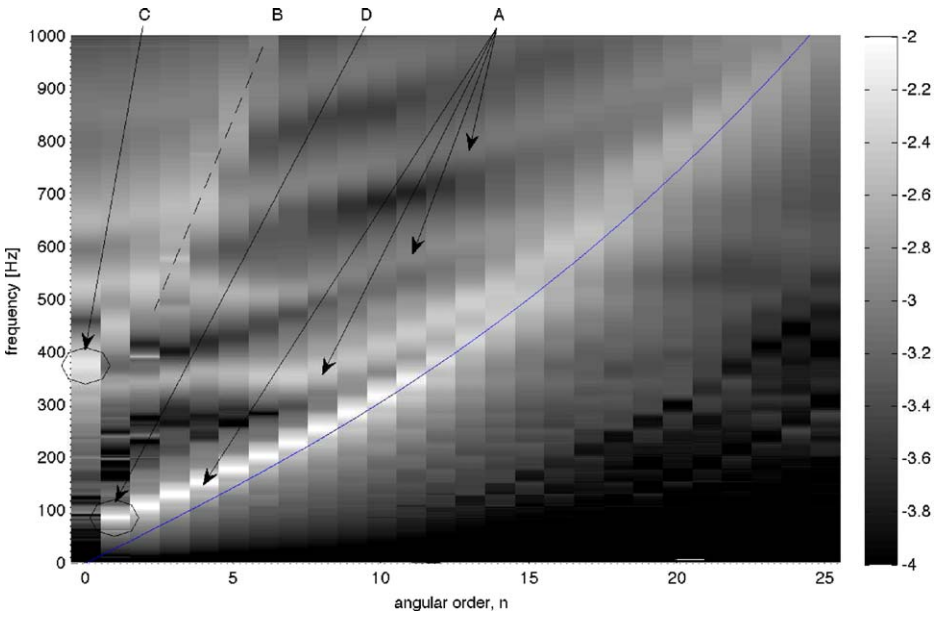


**Fig. 7.** Frequency–wavenumber map for central radial response to central radial forcing. The quantity plotted is $\log_{10}|i\omega\hat{w}(n,0,\omega)|$. Labelled features: *A*, bending wave branches; *B*, extensional wave 'wedge'; *C*, 'breathing' resonance; *D*, 'bounce' resonance. Also shown superposed is the one-dimensional flat-plate bending wave dispersion relation, (75), for parameter values $R=0.346\,\mathrm{m}$, $M=19.2\,\mathrm{kg\,m^{-2}}$, $t_i=76\,100\,\mathrm{N\,m^{-1}}$, $b_{22}=16\,\mathrm{N\,m}$.

### 3.3. Data analysis

Transfer functions were obtained by averaging 20 ratios of Fourier transforms of the output velocity response and input force. Each Fourier transform was estimated by application of the fast Fourier transform to an 8192 point data record, multiplied by the associated Hanning window, giving a frequency resolution of 1 Hz. There was no overlap between adjacent records. These transfer functions are also commonly referred to in the literature as 'mobilities'; they correspond to $i\omega[\tilde{u}\ \ \tilde{v}\ \ \tilde{w}]$, where $(\tilde{u},\tilde{v},\tilde{w})$ are the single Fourier transforms (with respect to time) of the impulse response components $(u,v,w)$.

Bolton et al. [19] have shown that a wavenumber decomposition of the spatial response variation yields valuable insight. In our case, it is also useful because it provides a direct comparison with the Fourier-transformed quantities calculated from the theoretical model. For a given set of transfer functions $i\omega\tilde{w}(\theta,l,\omega)$ say, the Fourier series coefficients $i\omega\hat{w}(n,l,\omega)$ were estimated by mirroring the transfer functions in azimuthal angle (preliminary checks having confirmed the validity of this symmetry assumption) and then applying a discrete Fourier transform to the complete set.

### 3.4. Sample results

The general form of transfer functions between radial forcing and response is already well established (see, for example, [4,5,11,19]). Thus, here, we restrict attention to the frequency-wavenumber map for central forcing and response (Fig. 7). The features identified by Bolton et al. [19] are clearly evident: a number of bending-wave branches (A) and an extensional-wave 'wedge' (B). Also visible are the 'breathing' resonance (C), and the 'bounce' mode (D), the latter corresponding to near-rigid-body motion of the tyre belt, with restoring force provided by the sidewalls. Finally, the sharp local peaks at frequencies $195m\,\mathrm{Hz}$ (for $m=1-3$) correspond to acoustic cavity modes. (Note that their presence casts some doubt on our neglect of cavity/belt coupling. This issue is deferred to future studies of force transmissibility to the hub.) The interpretative value of the frequency-wavenumber map is clear; in the following section we shall see that it is also helpful for parameter estimation.

## 4. Parameter estimation

The long-term aim of this work is to develop an entirely predictive model. We therefore seek to minimise the number of parameters that are adjusted in order to match calculations and experiment. The following section thus considers which variables can be determined *a priori*, either from basic measurements on an existing tyre (as in the current example) or from early design information. We then move on to consider the adjustable parameters. These are sufficiently numerous to prohibit a numerical search of all possible combinations for a best fit, and preliminary investigations with more advanced optimisation algorithms gave discouraging results. A directed approach, which concentrates on setting small groups of

parameters to match specific features of the frequency-wavenumber map, was therefore developed. The nature of this method makes it probably generalisable across different tyres and, for this reason, it is described in detail. Finally, we conclude with a comparison of model predictions and experiment for excitation/response combinations not used in the fitting process.

### 4.1. Fixed parameters

#### 4.1.1. Geometrical parameters

The geometrical parameters required by the model are the belt width and radius, $b$ and $R$, and the sidewall radius, rim angle and belt angle, $R_s$, $\phi_r$ and $\phi_b$. The belt/sidewall junction on a real tyre is not unambiguously identifiable; we define it as the edge of the steel reinforcing elements. Measurements on the inflated tyre and on cut elements then give $b=201$ mm, $R=346$ mm. (Note that, due to cross-belt curvature, the distance of the steel from the axis increases to 352 mm at the belt centre.)

The sidewall geometry is less straightforward to measure. The first consideration is the location of the rim 'end' which, due to the constraining effect of the rim cannot simply be taken as the bead. Instead, we define it to be at the intersection of the radial plies and the top of the rim protector, or 'chafer', region. This sets the sidewall height, $H_s$, and rim inwards displacement, $d_r$, where (see Fig. 4)

$$H_s = R_s[\sin\phi_b + \sin\phi_r], \quad d_r = R_s[\cos\phi_b - \cos\phi_r]. \tag{72}$$

The angles $\phi_b$ and $\phi_r$ are now determined once $R_s$ is known. This parameter is left adjustable. The measured values of $H_s$ and $d_r$ are given in Table 1.

#### 4.1.2. Mass parameters

The belt mass density, $M$, can be found by weighing a cut piece. The corresponding sidewall parameter, $M_s$, is less easily accessible, because the sidewall arc length $l_s = R_s(\phi_b + \phi_r)$ is hard to determine with accuracy. We therefore specify the product $M_s l_s$, the sidewall mass per unit belt circumference, which is estimated using a sidewall piece obtained from two radial cuts. The values found for $M$ and $M_s l_s$ are given in Table 1.

#### 4.1.3. Mean tensions

The circumferential tensions in both belt and sidewall have already been defined in terms of the inflation pressure, $p_i$, and the respective radii of curvature. The axial belt tension, $s_i$, however, remains undetermined. At this point, we recall the deferred issue of steady force continuity at the belt/sidewall junction. This condition implies that

$$s_i = t_s \sin\phi_b = p_i R_s \sin\phi_b, \tag{73}$$

i.e. the axial tension is the inflation pressure multiplied by approximately half the sidewall height. The exact value will thus depend on the adjustable parameter $R_s$ but, for the test inflation pressure of 2.2 bar, it is approximately 11 kN m$^{-1}$. This is markedly lower than estimated by Andersson and Larsson [5], who use 42 kN m$^{-1}$ (a value taken equal to the circumferential tension, which itself is tuned to fit their data, and hence is lower than expected for their tyre radius) for the first bending branch, 88 kN m$^{-1}$ for the second and 63 kN m$^{-1}$ for the third.

There remains an unbalanced steady radial component $t_s\cos\phi_b$. We view the associated belt stress and strain fields as perturbations to the mean state defined in Section 2. The linearity of our formulation then implies that this steady solution is independent of the vibrations, i.e. the two are simply superposed. Our unsteady measurements thus pick out solely the vibrational solution developed in Section 2.3.

### 4.2. Adjustable parameters

One geometrical parameter, the sidewall radius, was left variable in the preceding section; once set, its value determines the axial belt tension, $s_i$, and the sidewall angles ($\phi_r$, $\phi_b$), mass per unit area ($M_s$) and tension ($t_s$). This leaves the elastic constants for the belt and sidewall as the other parameters to be found on the basis of comparison with experiment.

**Table 1**
Parameters fixed by physical considerations.

| | |
|---|---|
| Belt width, $b$ (m) | 0.201 |
| Belt radius, $R$ (m) | 0.346 |
| Sidewall height, $H_s$ (m) | 0.104 |
| Sidewall rim displacement, $d_r$ (m) | 0.002 |
| Belt mass density, $M$ (kg m$^{-2}$) | 19.2 |
| Sidewall mass density, $M_s l_s$ (kg m$^{-1}$) | 0.788 |
| Inflation pressure, $p_i$ (N m$^{-2}$) | $2.2\times10^5$ |
| Belt mean circumferential tension, $t_i$ (N m$^{-1}$) | 76 100 |

First, we must address the hitherto-neglected issue of damping. Damping is represented by adding an imaginary loss factor to the elastic constants, e.g.

$$a_{22}^{(C)} = a_{22}(1+i\eta_a). \tag{74}$$

In order to allow for different damping mechanisms in extensional and bending motions, we also introduce $\eta_b$, which applies to the elastic constants $b_{11}$, $b_{22}$, $b_{12}$, $h_{12}$, and to the belt tensions, $t_i$ and $s_i$. Similarly, $\eta_{as}$ and $\eta_{bs}$ apply to the corresponding sidewall parameters, $a_s$ and $t_s$. Lastly, the sidewall circumferential stiffness, $k_\theta$, has loss factor $\eta_\theta$.

We now describe a systematic approach to estimating the variable parameters. This starts with the sidewall circumferential stiffness, then considers the loss factors, then derives a workable set of elastic parameters assuming isotropy, next sets the sidewall radius, and finally introduces anisotropy. Note that our formulation, in principle, admits frequency dependence in these parameters, a phenomenon that is known to be important in rubber. Nonetheless, to fulfil our aim of minimising the number of empirical variables, we choose to keep them constant. This approach may be partially justified on the basis that the frequency dependence in the stiffer belt elements (steel and cords) is likely to be less significant. However, it must finally stand or fall by the success of the model's predictions.

#### 4.2.1. Sidewall circumferential stiffness

Fig. 8 shows the transfer function between circumferential forcing and circumferential response at the same location. The resonance peaks for the first three Fourier orders have been identified by reference to the relative phases of this, the 90° and the 180° transfer functions. The $n=0$ peak corresponds to the (almost) rigid-body rotation mode analysed in Appendix A. Its frequency is 53.5 Hz. Although the associated value for $k_\theta$ depends on $g_{12}$, $h_{12}$ and $s_i$, the values that we subsequently find for these parameters imply that it is close to the rigid-body limit given by Eq. (86), i.e. $k_\theta = 2.2\times10^5\,\mathrm{Nm}^{-2}$. This is a factor of 10 smaller than the typical static radial stiffness found in Section 2.2.2, confirming our earlier assertion to this effect.

#### 4.2.2. Loss factors

A standard characterisation of damping is via the 'half-power bandwidth', $\Delta f/f_0$, where $f_0$ is the frequency of a resonance peak, and $\Delta f$ is its half-power width; i.e. the frequency range over which its amplitude is greater than $1/\sqrt{2}$ times the peak height. It is straightforward to show that this characterisation is linked to the loss-factor representation, Eq. (74), by $\Delta f/f_0 = \eta_a$. Approximate estimates of the loss factors are thus straightforward to obtain from the measured transfer functions. For example, the 'rigid-body rotation' peak identified in Fig. 8 yields a damping factor $\eta_\theta = 0.04$. The other damping factors are not as unambiguously associated with specific resonances so, at this stage, they are all assigned

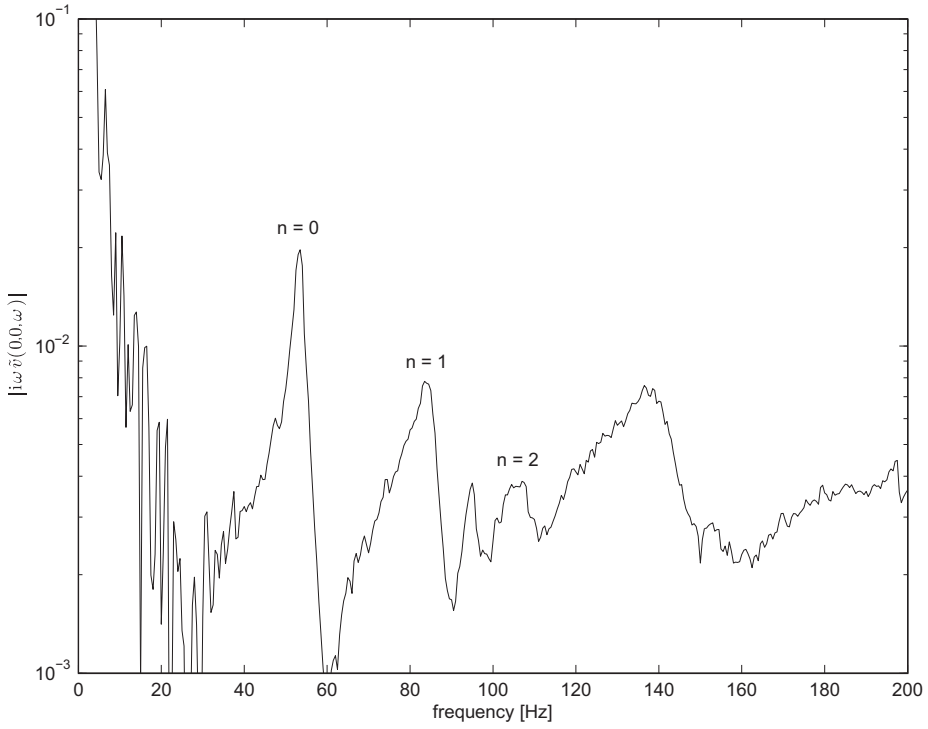


**Fig. 8.** Central circumferential response to circumferential forcing at the same location. Fourier orders associated with resonance peaks have been identified from phases of the corresponding response at 90° and 180° separation. (Note expanded frequency scale.)

the same value. Since our measured half-power bandwidths typically lie in the region 0.06–0.09, we set $\eta_a = \eta_b = \eta_{as} = \eta_{bs} = 0.075$.

*4.2.3. Circumferential bending stiffness*

Perhaps the most salient feature of the experimental frequency-wavenumber plot (Fig. 7) is the first bending branch. At higher values of $n$, one would expect this to be dominated by stiffnesses associated with circumferential variations, and to be independent of curvature. In this case, Eq. (20) reduces to the flat-plate result

$$M\omega^2 = b_{22}\left(\frac{n}{R}\right)^4 + t_i\left(\frac{n}{R}\right)^2. \tag{75}$$

As the only unknown parameter here is $b_{22}$, it is possible to seek the value that most closely matches the measurements. Fig. 7 shows the resulting curve, overlaid on the experimental map, for $b_{22} = 16\,\mathrm{Nm}$. Once the stiffening effect of curvature is no longer evident (from about $n = 9$ upwards), the match is excellent. (One could argue that the frequencies are slightly overpredicted for $n \geq 20$. Since, however, this is a region where rotational inertia might be expected to bring measured values below the theory, this discrepancy was tolerated for the sake of optimum agreement in the $n = 10-15$ range.)

*4.2.4. Extensional stiffnesses*

In Appendix A, it is shown that the 'breathing' frequency is approximately determined by the extensional stiffness parameters $a_{22}$, $a_{12}$ and $a_{11}$. Since the analysis is not exact, we choose their values by matching the calculated and measured breathing peaks. This approach necessitates a provisional complete parameter set. It is provided by assuming that the isotropic relations (14), (15) between the elastic constants apply, and that the effective Poisson's ratio is 0.4 (a value taken from experiments on uniaxial composites with components representative of those in a tyre belt [20]). The sidewall extensional stiffness is set equal to $a_{11}$, with $\eta_{as} = \eta_a$. Finally the sidewall radius is set equal to the sidewall height, 0.104 m (implying that $\phi_r$ and $\phi_b$ are about 30°). This leaves two free variables for the matching: $a_{22}$ and $\eta_a$.

Fig. 9 shows the experimental and (matched) numerical results for $n = 0$, the latter with $a_{22} = 15 \times 10^6\,\mathrm{N\,m^{-1}}$ and $\eta_a = 0.1$. It has proved possible to reproduce the height, location and breadth of the breathing peak with remarkable fidelity. The higher peaks, on the other hand, are currently not well predicted.

At this stage, we can consider the accuracy of the breathing frequency estimates of Section A.3. Neglecting the sidewall impedance in Eq. (93) gives 373 Hz, while representing it with the full sidewall mass gives 314 Hz. One would expect these estimates to bound the observed value. In fact, the latter is 376 Hz. This is because the experimental peak is a merger of the 'true' breathing resonance with the next $n = 0$ resonance. (We assert this for two reasons: first, numerical simulations for

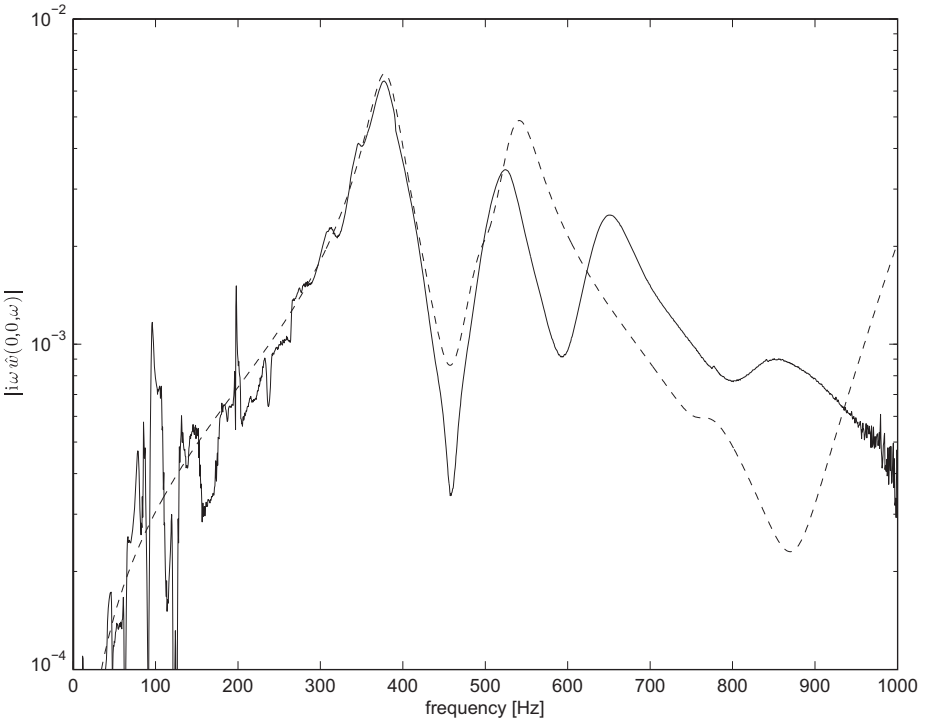


**Fig. 9.** $n = 0$ component of frequency-wavenumber map: —, measured; – –, calculated. Variable parameter values: $a_s = a_{11} = a_{22} = 15 \times 10^6\,\mathrm{N\,m^{-1}}$, $a_{12} = 6 \times 10^6\,\mathrm{N\,m^{-1}}$, $g_{12} = 4.5 \times 10^6\,\mathrm{N\,m^{-1}}$, $b_{11} = b_{22} = 16\,\mathrm{N\,m}$, $b_{12} = 6.4\,\mathrm{N\,m}$, $h_{12} = 19.2\,\mathrm{N\,m}$, $\eta_a = \eta_{as} = 0.1$, $\eta_b = \eta_{bs} = 0.075$, $\eta_\theta = 0.04$, $R_s = 0.104\,\mathrm{m}$.

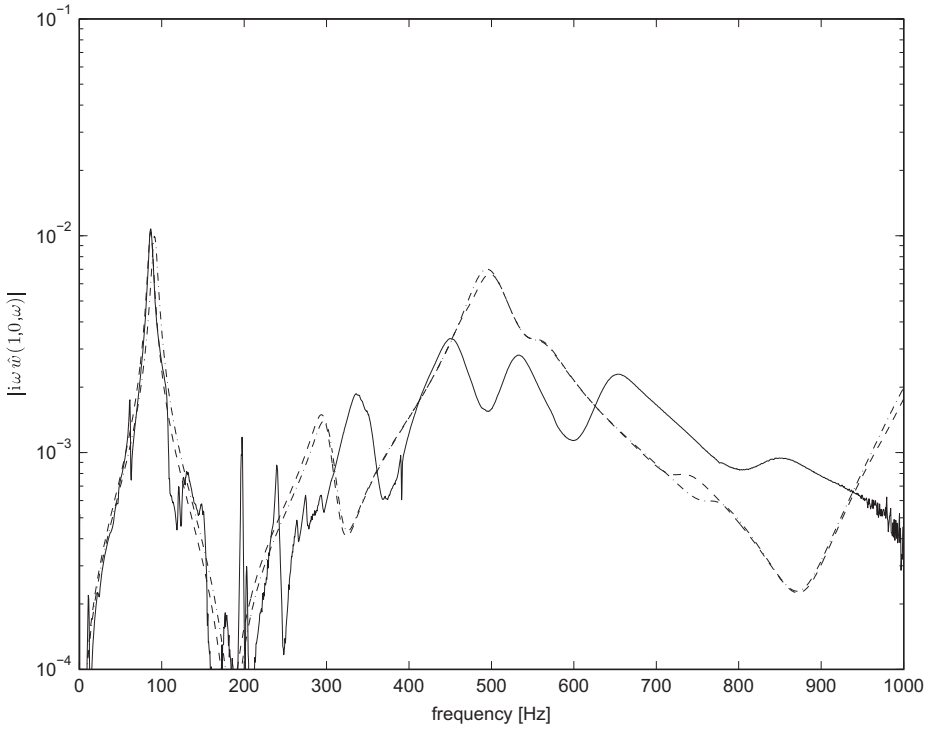


**Fig. 10.** $n=1$ component of frequency-wavenumber map: —, measured; – –, calculated ($R_s=0.095$ m); – · –, calculated ($R_s=0.104$ m). Other variable parameters as Fig. 9.

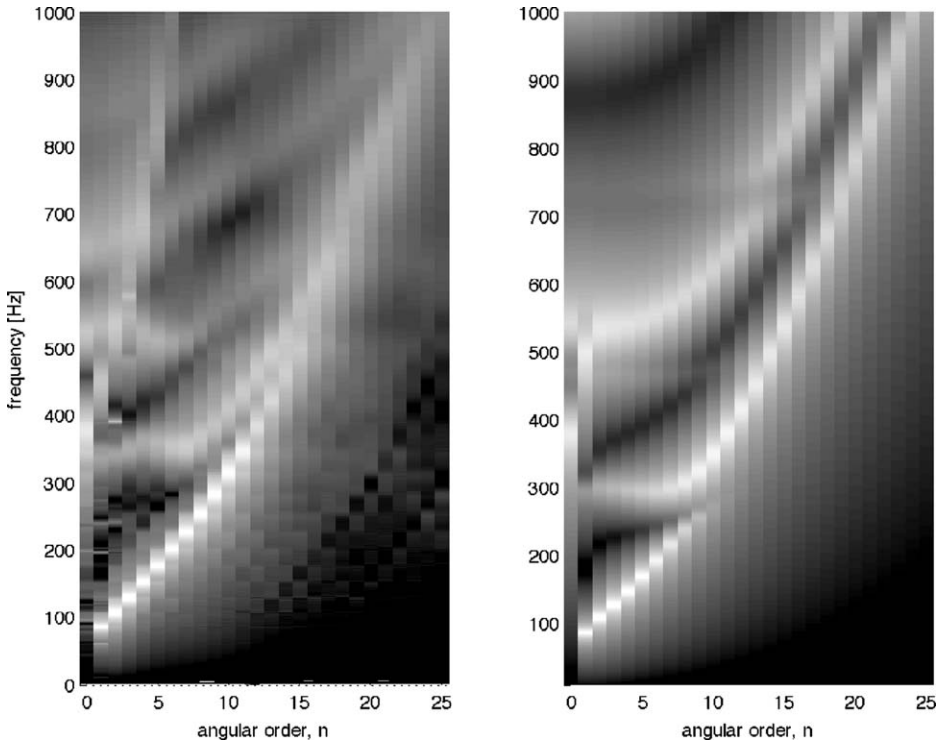


**Fig. 11.** Comparison of measured (left) and calculated (right) frequency-wavenumber maps, for isotropic parameter set. Variable parameters as Fig. 9 except for $R_s=0.095$ m. Greyscale levels correspond to Fig. 7.

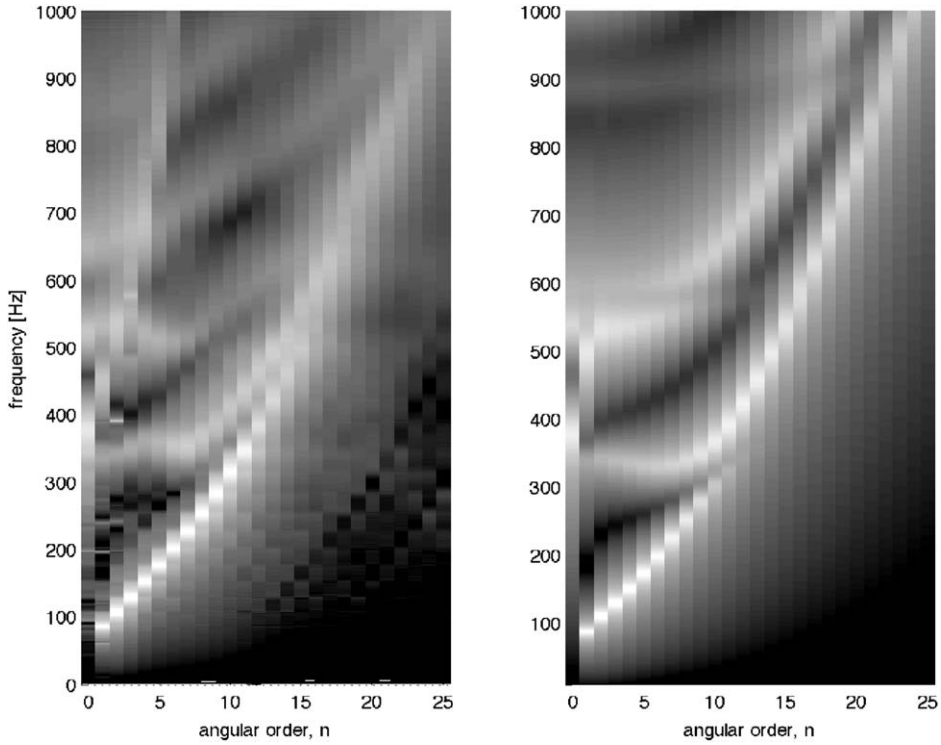


**Fig. 12.** Comparison of measured (left) and calculated (right) frequency-wavenumber maps for isotropic parameter set and reduced sidewall mass. Variable parameter values: $a_s = a_{11} = a_{22} = 14.8 \times 10^6\,\mathrm{N\,m^{-1}}$, $a_{12} = 5.9 \times 10^6\,\mathrm{N\,m^{-1}}$, $g_{12} = 4.4 \times 10^6\,\mathrm{N\,m^{-1}}$, $b_{11} = b_{22} = 16\,\mathrm{N\,m}$, $b_{12} = 6.4\,\mathrm{N\,m}$, $h_{12} = 19.2\,\mathrm{N\,m}$, $\eta_a = \eta_{as} = 0.1$, $\eta_b = \eta_{bs} = 0.075$, $\eta_\theta = 0.04$, $R_s = 0.095\,\mathrm{m}$. Sidewall mass scaled by 0.66. Greyscale levels correspond to Fig. 7.

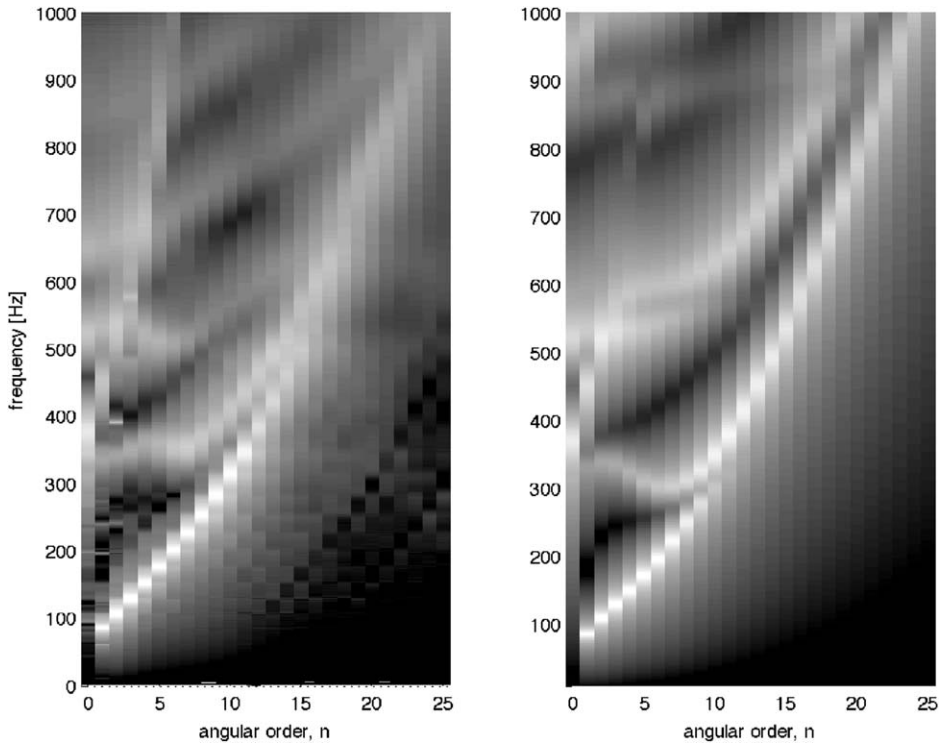


**Fig. 13.** Comparison of measured (left) and calculated (right) frequency-wavenumber maps for anisotropic parameter set. Variable parameter values: $a_s = a_{11} = 2.9 \times 10^6\,\mathrm{N\,m^{-1}}$, $a_{22} = 20 \times 10^6\,\mathrm{N\,m^{-1}}$, $a_{12} = 4.7 \times 10^6\,\mathrm{N\,m^{-1}}$, $g_{12} = 8.8 \times 10^6\,\mathrm{N\,m^{-1}}$, $b_{11} = 13.5\,\mathrm{N\,m}$, $b_{22} = 16\,\mathrm{N\,m}$, $b_{12} = 6.4\,\mathrm{N\,m}$, $h_{12} = 19.2\,\mathrm{N\,m}$, $\eta_a = \eta_{as} = 0.1$, $\eta_b = \eta_{bs} = 0.075$, $\eta_\theta = 0.04$, $R_s = 0.095\,\mathrm{m}$. Sidewall mass scaled by 0.66. Greyscale levels correspond to Fig. 7.

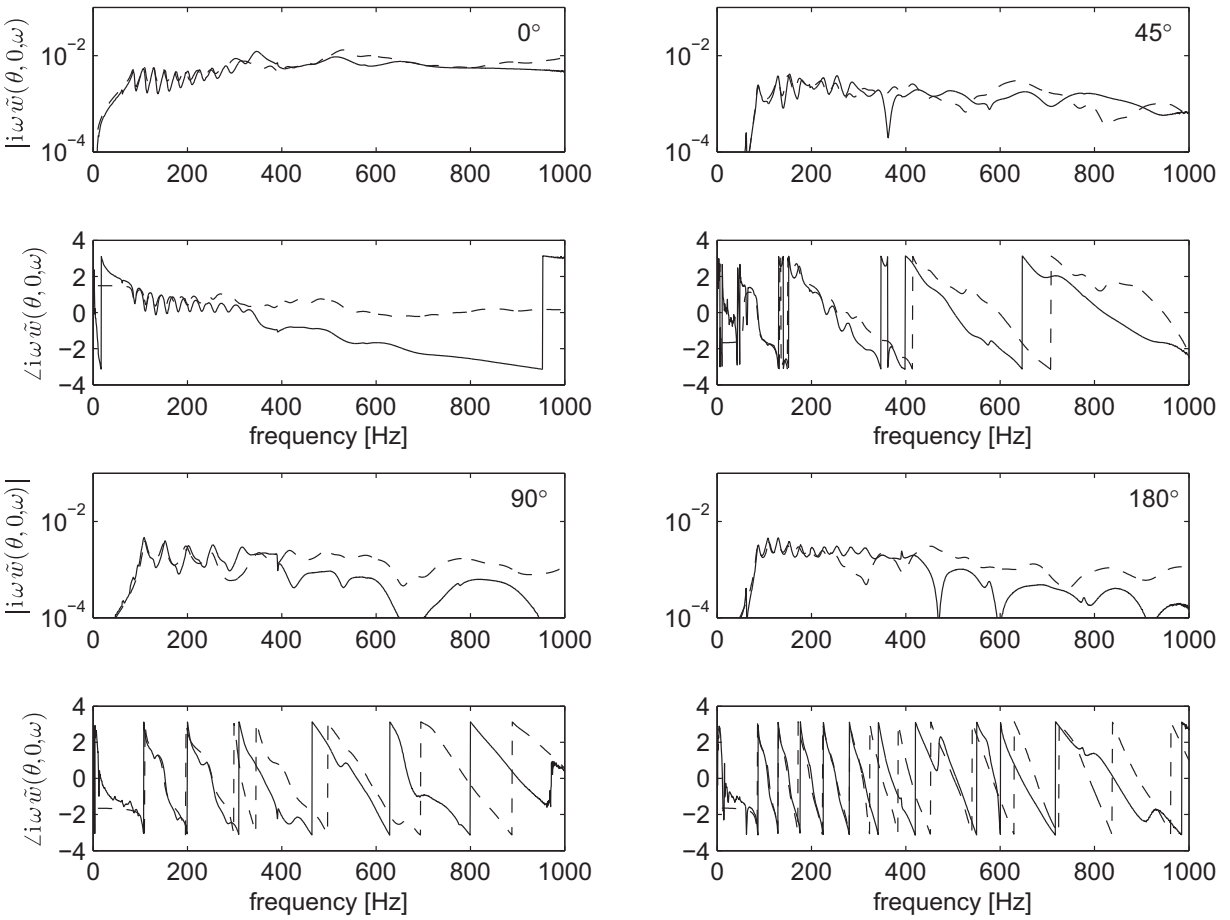


**Fig. 14.** Radial/radial transfer functions for central response to central forcing at varying azimuthal separations (labelled): —, measured; – –, calculated from map of Fig. 13.

lower $a_{22}$ values show two peaks; second, there is only one $n=0$ peak associated with the first two bending branches visible in Fig. 7.) This feature may well be specific to our particular tyre. In any case, the predicted resonance frequencies are sufficiently accurate to justify the use of Eq. (93) in obtaining an initial estimate of $a_{22}$ for the fitting process.

*4.2.5. Sidewall radius*

The main influence of the sidewall radius is on the static sidewall stiffness, which was shown in Section 2.2.2 to be highly sensitive to the sidewall angle. In turn, we expect the sidewall stiffness to be most significant for (almost) rigid-body belt motions. The particular instance that is visible in measurements of belt radial velocity is the 'bounce' mode, with $n=1$. This mode is visible in the experimental map at 87 Hz, and the sidewall radius is set so that the calculated location is identical. The predominance of sidewall flexure in this motion implies that its damping is determined by $\eta_{bs}$, which is thus also set at this stage.

Fig. 10 shows the measured and calculated map components for $n=1$. Two calculated curves are plotted, the first for the original choices of $R_s$ and $\eta_{bs}$ (0.104 m and 0.075) and the second for the matched values (0.095 m and 0.075). Again, excellent agreement with the target peak is achieved, but higher peaks are not well reproduced. In particular, the second resonance frequency is under-predicted. This discrepancy is not confined to the $n=1$ component, as can be seen from Fig. 11, which compares the experimental and predicted maps for the parameter set at this stage (using the same greyscale levels as Fig. 7); the second symmetric bending branch sits between 300 and 400 Hz for $n$ up to about 8, while its predicted location is at 300 Hz or slightly below.

While it is tempting to ascribe the error to the assumption of isotropy in determining the elastic constants, numerical investigations suggest that this is not the case; with $a_{22}-a_{12}^2/a_{11}$ held fixed (to maintain the breathing frequency match) it has been found impossible to shift the branch up significantly. It is, however, sensitive to the value of the sidewall mass; Fig. 12 shows the comparison with experiment when $M_s$ is reduced by a factor of 0.66 (chosen so that experimental and calculated peaks match at $n=1$ and 2) and $a_{22}$ is reduced from $15\times10^6$ to $14.8\times10^6$ N m$^{-1}$ to preserve the breathing peak location. Although there remain differences for $n=3$ and above, the agreement is much better. Justification for reducing

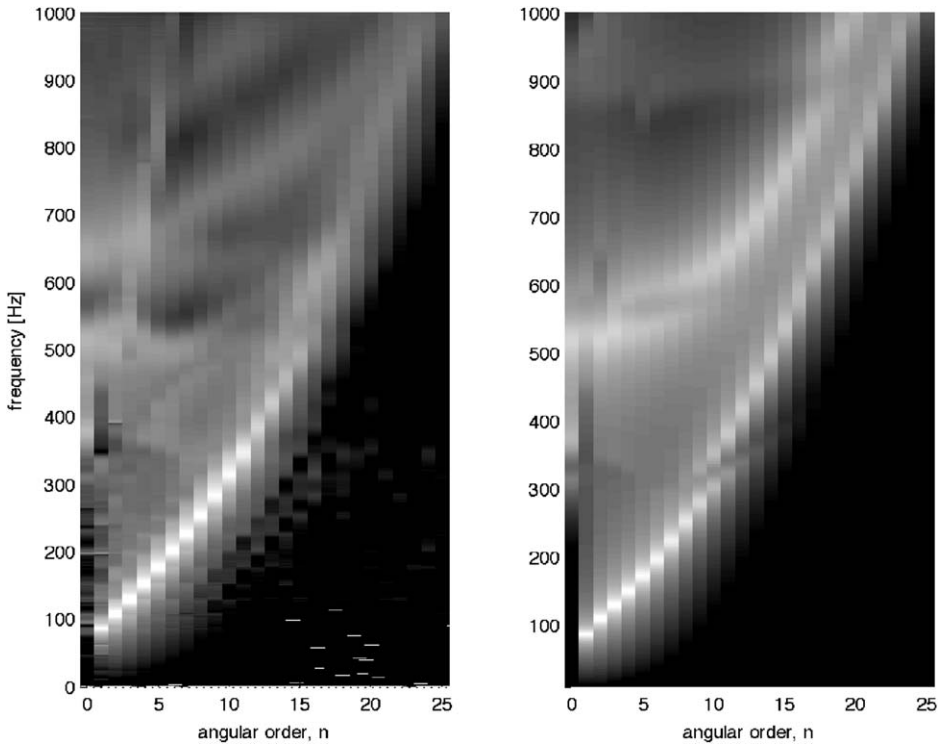


**Fig. 15.** Comparison of measured (left) and calculated (right) frequency-wavenumber maps; radial response 6 cm off centre to radial forcing at centre. Parameters as Fig. 13. Greyscale levels correspond to Fig. 7.

the sidewall mass may be provided by the observation that it is non-uniformly distributed, with maximum thicknesses near the ends, which will be less involved in the relevant motions. An estimate of the effective mass reduction expected on the basis of the static displacement shape found in Section 2.2.2 is made in Appendix B. The value found is 0.92. Although imperfect, this calculation is an improvement on the original assumption, and might thus be of use for purely predictive application of the model.

The calculated map of Fig. 12 represents the best agreement found under the isotropic assumption. Up to 500 Hz, it is generally good and, indeed, might well be satisfactory for modelling purposes without further refinement. However, it is clearly deficient in two important respects: the frequencies of the higher bending branches are grossly over-predicted, and the in-plane 'wedge' is effectively absent. We therefore now consider whether better agreement is possible if $a_{12}$, $a_{11}$, $g_{12}$, $b_{11}$, $b_{12}$ and $h_{12}$ are no longer linked to $a_{22}$ and $b_{22}$ by the isotropic relations.

*4.2.6. Anisotropic elastic constants*

The starting point for this stage is the (empirical) observation that the $n=0$ peak at 540 Hz is essentially unaffected by the values of $a_{11}$, $a_{12}$ and $a_{22}$ as long as $a_{22}-a_{12}^2/a_{11}$ is maintained constant. The only remaining elastic parameter in the $n=0$ equations is $b_{11}$, which is accordingly set so that the experimental peak location (at 520 Hz) is matched. This leads to a reduction in $b_{11}$ from 16 to 13.5 N m.

On the other hand, $a_{11}$, $a_{12}$ and $a_{22}$ are found to have a significant effect on the $n=1$ peak between 400 and 500 Hz. It is thus possible to find a series of $(a_{22}, a_{11}, a_{12})$ sets that satisfy the breathing frequency matching condition, $a_{22}-a_{12}^2/a_{11}=12.4\times10^6\,\mathrm{N\,m^{-1}}$, and also place this peak at its experimental location (450 Hz). Furthermore, with any of these sets the calculation now reproduces the in-plane wedge. However, at lower values of $a_{22}$, the dip in the second symmetrical bending branch around $n=5$ becomes more pronounced, while at higher values the third symmetrical bending branch is overly stiffened. The set $a_{22}=20\times10^6\,\mathrm{Nm^{-1}}$, $a_{11}=2.9\times10^6\,\mathrm{Nm^{-1}}$, $a_{12}=4.7\times10^6\,\mathrm{Nm^{-1}}$ was found to provide a reasonable compromise.

The remaining in-plane elastic parameter, $g_{12}$, was now found to have little influence. Doubling it from its original value of $4.4\times10^6\,\mathrm{Nm^{-1}}$ did, however, slightly mitigate the second branch dip; a further doubling had no effect. It was thus set to $8.8\times10^6\,\mathrm{Nm^{-1}}$.

Finally, the dependence of the map on the bending stiffnesses $b_{12}$ and $h_{12}$ was found to be imperceptible when they were increased or decreased by a factor of 2. They were therefore left at their original values, $b_{12}=6.4$ Nm and $h_{12}=19.2$ Nm.

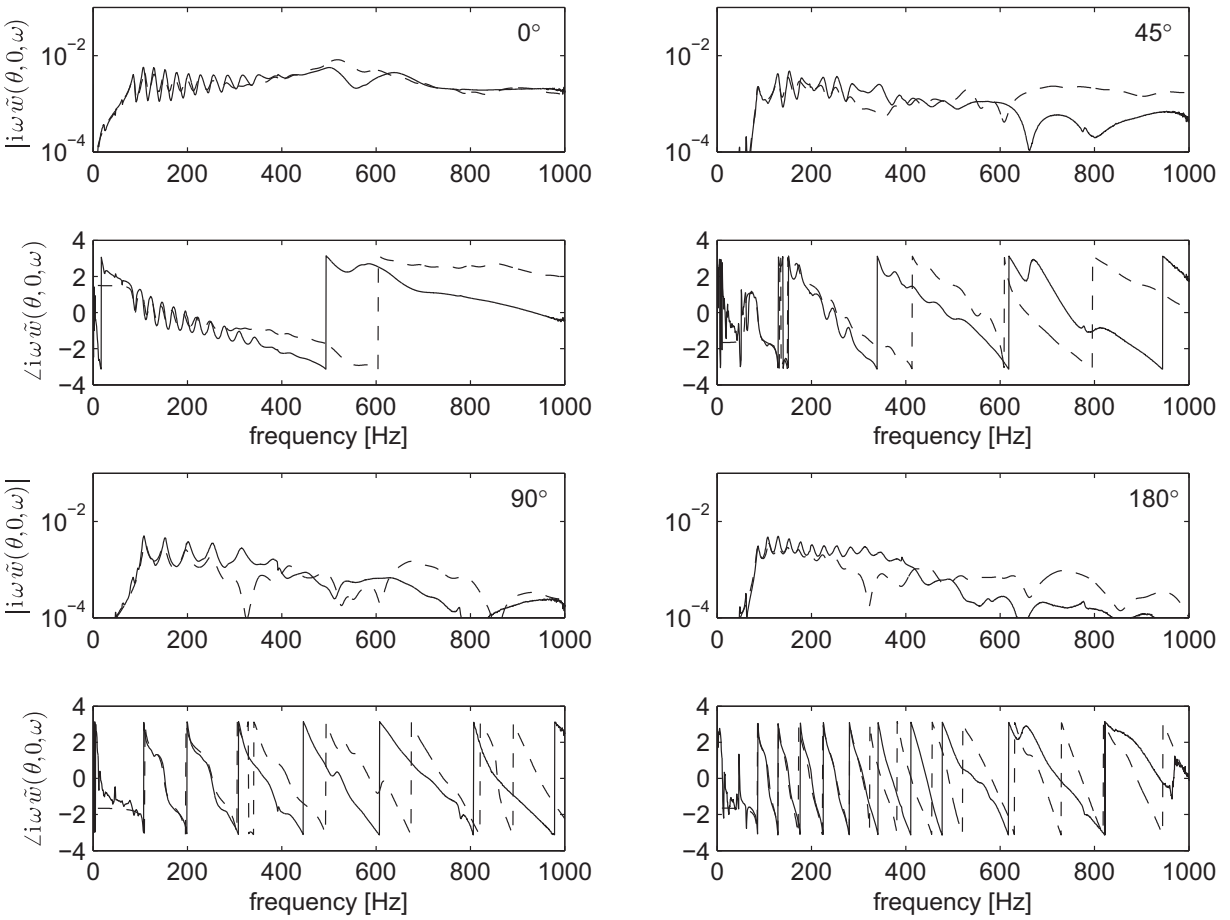


**Fig. 16.** Radial/radial transfer functions for off-central response to central forcing at varying azimuthal separations (labelled): —, measured; – –, calculated from map of Fig. 15.

Fig. 13 shows the new comparison with experiment. The most successful development is the emergence of the in-plane wedge. The drop in the third branch due to the reduction of $b_{11}$ is offset by a rise due to the increase in $a_{22}$, so it is still somewhat high for $n \geq 4$. Meanwhile, the increased second branch dip makes its agreement slightly worse than in the isotropic case.

In summary, although the anisotropic parameter set clearly reproduces the overall topology better, one would still question its accuracy above 500 Hz, while below 500 Hz it is not obviously superior to the isotropic set. Nevertheless, in this region, the agreement with experiment is good, particularly bearing in mind the correspondence in absolute levels.

### 4.2.7. *Individual transfer functions*

To assess the quality of the final fit more carefully, it is useful to compare specific transfer functions. Fig. 14 shows measured transfer functions for a range of angular separations between forcing and response, along with the predictions from the calculation (obtained from an inverse discrete Fourier transform over orders $n = 0-36$).

At 0° separation (i.e. the point mobility) the agreement is good up to about 300 Hz, after which discrepancies are evident in both magnitude and phase, with the experimental results showing more lag. In comparison, Andersson and Larsson's model [5] exhibits better fidelity in this region, but significant errors around their first resonance peak. Meanwhile Pinnington [11] finds agreement similar to ours, though still with some discrepancy at the first resonance.

Similar divergences above 300 Hz are found for responses away from the excitation point, and these can amount to much larger percentage differences in magnitude. In absolute terms, however, the errors are lower than the 0° case. Phase lags are consistently under-predicted for the 45° and 90° separations, but not at 180°. There is also some evidence of systematic over-prediction in magnitude at the higher frequencies. Both Andersson and Larsson and Pinnington give only one example of such a response; each of these similarly shows much greater percentage errors than its respective point mobility.

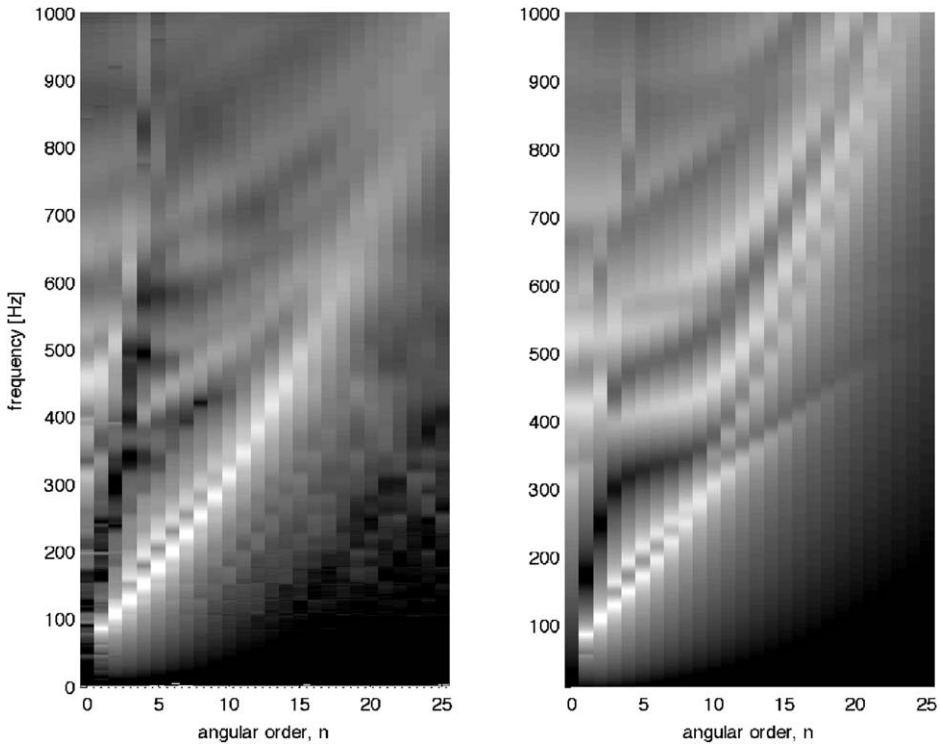


**Fig. 17.** Comparison of measured (left) and calculated (right) frequency-wavenumber maps; radial response 6 cm off-centre to radial forcing at same offset. Parameters as Fig. 13. Greyscale levels correspond to Fig. 7.

### 4.3. Other excitation/response combinations

Having specified a parameter set to match the case of central excitation and response, we now consider how well this set predicts two cases not used in the fitting. Fig. 15 shows the measured and predicted frequency-wavenumber maps for off-centre response to central forcing; samples of the corresponding transfer functions are given in Fig. 16. Figs. 17 and 18 present the same results for both forcing and response off centre.

The first noteworthy point is that overall levels, judged on the basis of the region to the right of the first bending branch, are again well predicted. Qualitative changes in the topology of the maps—specifically the near-absence of the second symmetric bending branch in both cases, and the appearance of two asymmetric bending branches for off-centre forcing—are also well reproduced. The discrepancies that can be observed in the maps correspond to those in Fig. 13, i.e. under-predicted resonance frequencies in the region 300–400 Hz, $n=5-10$, and fewer bending branches than measured above 600 Hz. Finally, the magnitude over-prediction seen at high frequencies in the transfer mobilities of Fig. 14 is evident in Figs. 16 and 18 as well.

### 4.4. Discussion

In the light of the frequency-wavenumber map comparisons, it is clear that our model captures the main physical features of the tyre vibration in this frequency range. Of the two discrepancies identified above, the over-prediction of bending resonance frequencies above 600 Hz is probably due to the neglect of belt thickness. A third wave type is unlikely yet to be cut on, but rotational inertia may well be important, and its inclusion would tend to lower the predicted bending branches in this region. In contrast, accounting for the frequency dependence of rubber stiffness would have the opposite effect.

The other discrepancy is the under-prediction of resonance frequencies between 300 and 400 Hz, for $n=5-10$. Given the observed influence of the sidewall mass correction, we suggest that the sidewall model may be insufficiently stiff in this region. If so, a two-dimensional model, including circumferential curvature, may be called for. The addition of bending stiffness is less likely to be beneficial, as it would affect lower wavenumbers too. Further investigation of this area is clearly necessary.

Likewise, the high-frequency transfer-mobility magnitude errors could, perhaps, be reduced by further model development. Here, we regard the introduction of frequency dependence into the loss factors as a promising approach. This, however, will only be attempted if we find that these errors have a significant effect on tyre rolling simulations.

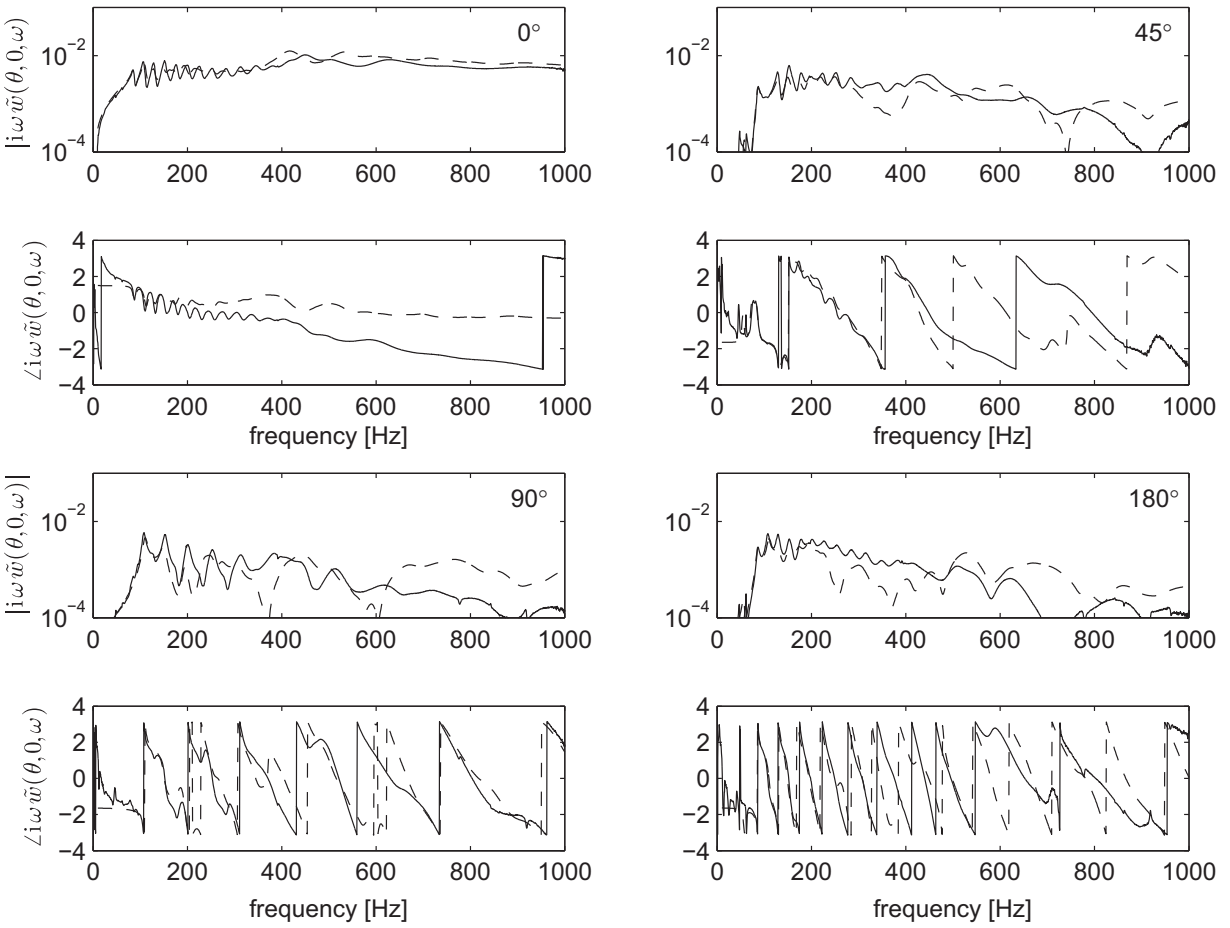


**Fig. 18.** Radial/radial transfer functions for off-central response to off-central forcing at varying azimuthal separations (labelled): —, measured; – –, calculated from map of Fig. 17.

Compared to the Kropp group's formulation [4,5], the improved low-frequency fidelity is a clear advantage in the context of our project. Both models require comparison with experiment in order to set their adjustable parameters properly; for design studies, however, ours has the advantage that several key parameters—circumferential tension, sidewall radius, sidewall tension, axial tension—can be set *a priori*. Depending on the application, this benefit might outweigh its poorer accuracy at the higher frequencies.

Less clear performance differences are evident when comparing the predictions of our model and Pinnington's [11]. Although we would hope that our more rigorous treatment of belt/sidewall coupling would lead to better accuracy when using elastic parameters derived *a priori*, rather than empirically, we have not yet reached the stage where this is possible. (Preliminary calculations, using laminar composite theory [21], showed significant differences from the values found here.) Thus, at present, the practical benefits are restricted to the reduction in adjustable parameters, due to the simpler belt and sidewall representations.

Finally, our model must also be assessed in the light of the excellent results attainable at the same frequencies by waveguide FEA [3]. These, however, require calculations on the order of an hour [3], as opposed to minutes. They also require detailed geometric and elastic parameter information that may not be available at the early stages of vehicle design. Even if it is, the use of a simpler model can provide a designer with valuable physical insight. Thus, although our approach cannot compete in detail accuracy, we believe that it represents a useful complement to FEA analyses.

## 5. Conclusions

In this paper, we have presented a new theoretical model for tyre vibrations, intended mainly for the 0–500 Hz range. The new model represents the tyre geometry and material properties more realistically than previous, similar contributions to the literature, while attempting to maintain their useful simplifying assumptions. As a result, many of the important model parameters can be calculated *a priori*, given knowledge of the tyre's basic geometry, mass distribution and inflation pressure.

Nonetheless, there remain some parameters that can only be identified via comparison with experimental data. (Of these, the most important are the belt in-plane and bending stiffnesses, and the associated damping factors.) We have therefore developed a systematic approach to their estimation, based on frequency-wavenumber decomposition of the radial response to radial point forcing.

The results show good correspondence between theory and experiment up to about 300 Hz, and fair agreement up to 1 kHz. The main discrepancies can be classified under two headings: (i) under-predicted higher-mode resonance frequencies between 300 and 400 Hz; and (ii) over-predicted resonance frequencies for all flexural modes above 600 Hz. The former may be due to the neglect of circumferential curvature in the sidewall representation, while the latter is probably associated with the influence of rotational inertia in the real belt motions. Overall, though, the fidelity of the model is sufficient to encourage its use in tyre rolling simulations, and this will be the immediate focus of our future work.

## Acknowledgements

It is a pleasure to recognise the help and support of our co-workers on this project: Andy Bridgwater, Edwin Deerenberg, Malcolm Hardy, Jan Leyssens, Feiyang Liu, Dave Marshall, Nigel Taylor, Michael Sutcliffe and Frederic Wullens. We have also had useful discussions on shell theory with Paul Barbone, Ann Dowling, Greg McDaniel and Jim Woodhouse. The work is funded by the UK Engineering and Physical Sciences Research Council (Grant EP/D011035/1) and by Jaguar Cars Ltd.

## Appendix A. The axisymmetric modes of motion

### A.1. Introduction

Although the belt governing equations presented in this paper do not admit a general analytical solution, useful progress can be made when there is no rotation and the motions are axisymmetric. In this case, unforced vibrations correspond to solutions of the form $[u\ \ v\ \ w]=[\hat{u}(l)\ \ \hat{v}(l)\ \ \hat{w}(l)]\mathrm{e}^{\mathrm{i}\omega t}$. The equations of motion, (18)–(20), become

$$\left[M\omega^2+a_{11}\frac{\mathrm{d}^2}{\mathrm{d}l^2}\right]\hat{u}+\left(\frac{a_{12}}{R}-p_i\right)\frac{\mathrm{d}\hat{w}}{\mathrm{d}l}=0, \tag{76}$$

$$\left[M\omega^2+\left(g_{12}+\frac{9h_{12}}{16R^2}+s_i\right)\frac{\mathrm{d}^2}{\mathrm{d}l^2}\right]\hat{v}=0, \tag{77}$$

$$-\left(\frac{a_{12}}{R}-p_i\right)\frac{\mathrm{d}\hat{u}}{\mathrm{d}l}+\left[M\omega^2-b_{11}\frac{\mathrm{d}^4}{\mathrm{d}l^4}+s_i\frac{\mathrm{d}^2}{\mathrm{d}l^2}-\frac{a_{22}}{R^2}+\frac{p_i}{R}\right]\hat{w}=0, \tag{78}$$

and the boundary stress resultants, (21)–(24), are now given by

$$f_u=\left[a_{11}\frac{\mathrm{d}\hat{u}}{\mathrm{d}l}+\left(\frac{a_{12}}{R}-\frac{p_i}{2}\right)\hat{w}\right]\mathrm{e}^{\mathrm{i}\omega t}, \tag{79}$$

$$f_v=\left(g_{12}+\frac{9h_{12}}{16R^2}+s_i\right)\frac{\mathrm{d}\hat{v}}{\mathrm{d}l}\mathrm{e}^{\mathrm{i}\omega t}, \tag{80}$$

$$f_w=\left[\frac{p_i}{2}\hat{u}+\left(s_i\frac{\mathrm{d}}{\mathrm{d}l}-b_{11}\frac{\mathrm{d}^3}{\mathrm{d}l^3}\right)\hat{\omega}\right]\mathrm{e}^{\mathrm{i}\omega t}, \tag{81}$$

$$r_w=b_{11}\frac{\mathrm{d}^2\hat{w}}{\mathrm{d}l^2}\mathrm{e}^{\mathrm{i}\omega t}. \tag{82}$$

(Here, as for the general case, the constant contribution to $f_u$ has been omitted on the basis that it is associated with the equilibrium boundary loading.) These equations exhibit the unique feature of the axisymmetric motions: azimuthal displacements are decoupled from radial and axial. We start by considering the former.

### A.2. Azimuthal motions

The mode of interest for the parameter identification procedure is the lowest, which will be symmetric about $l=0$. The solution to Eq. (77) that has this form is

$$\hat{v}(l)=\hat{V}\cos\kappa_v l, \tag{83}$$

where $\hat{V}$ is an arbitrary constant, and

$$\kappa_v^2 = \frac{M\omega^2}{g_{12} + \dfrac{9h_{12}}{16R^2} + s_i}. \tag{84}$$

The sidewall boundary condition is $f_v = \mp k_\theta v$ at $l = \pm b/2$, so

$$\left(g_{12} + \frac{9h_{12}}{16R^2} + s_i\right)\kappa_v \tan\left(\frac{\kappa_v b}{2}\right) = k_\theta, \tag{85}$$

which (implicitly) specifies the resonance frequencies of the symmetric azimuthal modes. If $\kappa_v b/2 \ll 1$, this equation approximates to

$$M\omega^2 = \frac{2k_\theta}{b}, \tag{86}$$

which corresponds to pure rigid-body oscillations. Alternatively, given an observed first resonance frequency, $\kappa_v$ follows from Eq. (84), and Eq. (85) then provides the value of $k_\theta$ that is needed.

### *A.3. Radial and axial motions*

We are again concerned with the lowest resonance frequency, and thus make the assumption that the variation in $\hat{u}(l)$ and $\hat{w}(l)$ across the belt is small. They can then be expressed as series in ascending powers of $l$. For the symmetrical response that we seek, these take the form

$$\hat{u}(l) = \sum_{n=0}^{\infty} \hat{u}_{2n+1} l^{2n+1}, \quad \hat{w}(l) = \sum_{n=0}^{\infty} \hat{w}_{2n} l^{2n}. \tag{87}$$

An approximate solution follows by solving the system of equations to leading order. For Eq. (76) the $O(l)$ terms give

$$M\omega^2 \hat{u}_1 + 6a_{11}\hat{u}_3 + 2\left(\frac{a_{12}}{R} - p_i\right)\hat{w}_2 = 0, \tag{88}$$

while for Eq. (78), the $O(1)$ contribution is

$$-\left(\frac{a_{12}}{R} - p_i\right)\hat{u}_1 + \left(M\omega^2 - \frac{a_{22}}{R^2} + \frac{p_i}{R}\right)\hat{w}_0 + 2s_i\hat{w}_2 - 24b_{11}\hat{w}_4 = 0. \tag{89}$$

We represent the sidewall as a complex stiffness, approximated as zero in the axial direction, i.e. at $l = b/2$ we have $f_u = 0$, $f_w = -z_r w$ and $r_w = 0$. To leading order, these conditions become

$$a_{11}\hat{u}_1 + \left(\frac{a_{12}}{R} - \frac{p_i}{2}\right)\hat{w}_0 = 0, \tag{90}$$

$$\frac{p_i}{2}\hat{u}_1 + 2s_i\hat{w}_2 - 24b_{11}\hat{w}_4 = -\frac{2z_r}{b}\hat{w}_0, \tag{91}$$

$$\hat{w}_2 = 0. \tag{92}$$

These three equations allow us to express $\hat{u}_1$ and $\hat{w}_4$ in terms of $\hat{w}_0$, and the resonance frequency then follows directly from Eq. (89):

$$M\omega^2 = \frac{a_{22}}{R^2} - \frac{p_i}{R} - \frac{1}{a_{11}}\left(\frac{a_{12}}{R} - \frac{p_i}{2}\right)^2 + \frac{2z_r}{b}. \tag{93}$$

If $z_r$ is set to zero, the (negligible) inflation pressure terms neglected, and the isotropic forms for the stiffnesses substituted, this expression corresponds to that given by Calladine [22] for the 'ring frequency' of a narrow, isotropic cylinder. For non-zero $z_r$, the sidewalls represent an additional, distributed stiffness $2z_r/b$, corresponding to 'smearing' their contributions over the belt width.

In our example, the breathing resonance is above the first sidewall resonance frequency (calculated, from extension to dynamic motions of the analysis in Section 2.2.2, at 255 Hz), so $z_r$ will be negative, representing additional mass. As an upper limit, one could assume all the sidewall mass to be added, in which case $2z_r/b = -2M_s l_s\omega^2/b$. For the parameters in Table 1, $2M_s l_s/b$ is 7.8 kg m$^{-2}$, while $M$ is 19.2 kg m$^{-2}$. The accuracy of our approximation with these values is discussed in Section 4.2.4.

## Appendix B. Estimation of the effective sidewall mass

In Section 4.2.5, better agreement with experiment was found when the sidewall mass density was reduced from its measured value. It was argued that non-uniformity in the sidewall thickness was responsible for this effect.

To define an effective mass density for the sidewall, we require the kinetic energy of the equivalent, uniform-thickness sidewall to match that of the true, non-uniform sidewall in a given motion. At a given frequency, this condition implies a

**Table 2**
Measured sidewall thickness, $h_s$, as a function of arc length, $l$.

| $l$ (mm) | 0 | 5 | 15 | 25 | 35 | 45 | 55 | 65 | 75 | 85 | 95 | 105 | 110 |
|---|---|---|---|---|---|---|---|---|---|---|---|---|---|
| $h_s$ (mm) | 15 | 13 | 10 | 8 | 7 | 6.5 | 6 | 6.5 | 6.5 | 7 | 7 | 9 | 10 |

ratio of equivalent to actual mass density of

$$\frac{(\phi_b+\phi_r)\int_{-\phi_r}^{\phi_b} h_s(\phi)r_s(\phi)d_s^2(\phi)\mathrm{d}\phi}{\int_{-\phi_r}^{\phi_b} h_s(\phi)r_s(\phi)\mathrm{d}\phi\int_{-\phi_r}^{\phi_b} d_s^2(\phi)\mathrm{d}\phi}, \tag{94}$$

where $h_s(\phi)$ is the sidewall thickness and $d_s(\phi)$ its displacement. The variable $r_s(\phi)$ is the distance of the sidewall from the tyre axis; it arises because the volume of sidewall per unit belt circumferential distance decreases towards the rim, and is given by

$$r_s = R - R_s(\sin\phi_b - \sin\phi). \tag{95}$$

The measured sidewall thickness, as a function of arc length $l$ (from rim to belt) is given in Table 2. Note that the total measured arc length, $l_s$, is 110 mm; if this condition were added to the constraints in Section 4.1.1, $R_s$ would no longer be an adjustable parameter, and would be 95.5 mm (with $\phi_r = 34.1^\circ$, $\phi_b = 31.9^\circ$), remarkably close to the fitted value. However, small variations in $l_s$ correspond to much larger changes in $R_s$ and $\phi$, so it was decided not to rely on this measurement for parameter estimation. For the current calculation, we set $R_s = 95$ mm and $\phi_r = \phi_b = 33.2^\circ$. The displacement is approximated by the static results for a symmetrical sidewall, Eqs. (43)–(46), with the small term $p_i R_s/a_s$ neglected. The integrals in Eq. (94) were estimated via Simpson's rule, with discretisation corresponding to the measurements, giving a value of 0.92.

## References


[1] I. Lopez, R.E.A. Blom, N.B. Roozen, H. Nijmeijer, Modelling vibrations on deformed rolling tyres—a modal approach, *Journal of Sound and Vibration* 307 (2007) 481–494.
[2] S. Finnveden, M. Fraggstedt, Waveguide finite elements for curved structures, *Journal of Sound and Vibration* 312 (2008) 644–671.
[3] S. Finnveden, C.-M. Nilsson, M. Fraggstedt, Waveguide FEA of the vibration of rolling car tyres, *Proceedings of November*, Saint Raphael, 2005.
[4] K. Larsson, W. Kropp, A high-frequency three-dimensional tyre model based on two coupled elastic layers, *Journal of Sound and Vibration* 253 (2002) 889–908.
[5] P. Andersson, K. Larsson, Validation of a high frequency three-dimensional tyre model, *Acta Acustica united with Acustica* 91 (2005) 121–131.
[6] R.A.G. Graf, Tyre–road Interaction Noise, PhD Thesis, University of Cambridge, 2002.
[7] P. Campanac, K. Nonami, D. Duhamel, Application of the vibration analysis of linear systems with time-periodic coefficients to the dynamics of a rolling tyre, *Journal of Sound and Vibration* 231 (2000) 37–77.
[8] Y.-J. Kim, J.S. Bolton, Effects of rotation on the dynamics of a circular cylindrical shell with application to tire vibration, *Journal of Sound and Vibration* 275 (2004) 605–621.
[9] W. Soedel, *Vibrations of Shells and Plates*, third ed., Marcel Dekker, New York, 2004.
[10] R.J. Pinnington, A wave model of a circular tyre—part 1: belt modelling, *Journal of Sound and Vibration* 290 (2006) 101–132.
[11] R.J. Pinnington, A wave model of a circular tyre—part 2: side-wall and force transmission modelling, *Journal of Sound and Vibration* 290 (2006) 133–168.
[12] R.A.G. Graf, C.-Y. Kuo, A.P. Dowling, W.R. Graham, A mathematical model of tyre-road noise, *Institution of Mechanical Engineers* Paper C605/015/2002, 2002.
[13] J.L. Sanders Jr., An improved first-approximation theory for thin shells. NASA Langley Research Center, NASA-TR-R-24, 1959.
[14] T.L. Richards, Finite element analysis of structural–acoustic coupling in tyres, *Journal of Sound and Vibration* 149 (1991) 235–243.
[15] R. Courant, D. Hilbert, *Methods of Mathematical Physics*, Wiley, New York, 1989 (two volumes).
[16] C. Lecomte, W.R. Graham, A tyre belt model based on a 2D beam theory, University of Cambridge, Department of Engineering, CUED/A-AERO/TR28, 2007.
[17] C. Lecomte, W.R. Graham, D.J. O'Boy, Validation of a belt model for prediction of hub forces from a rolling tire, *Tire Science and Technology* 37 (2009) 62–102.
[18] R.J. Pinnington, Radial force transmission to the hub from an unloaded stationary tyre, *Journal of Sound and Vibration* 253 (2002) 961–983.
[19] J.S. Bolton, H.J. Song, Y.K. Kim, Y.J. Kang, The wave number decomposition approach to the analysis of tire vibration. *Proceedings of NOISE-CON 98*, Ypsilanti MI, April 1998, pp. 97–102.
[20] M. Kumar, C.W. Bert, Experimental characterization of mechanical behavior of cord-rubber composites, *Tire Science and Technology* 10 (1982) 37–54.
[21] F.L. Matthews, R.D. Rawlings, *Composite Materials: Engineering and Science*, Chapman & Hall, London, 1994.
[22] C.R. Calladine, *Theory of Shell Structures*, Cambridge University Press, Cambridge, 1983.